Comparative study on charge radii and their kinks at magic numbers

Tomoya Naito (内藤智也)[*]
RIKEN Interdisciplinary Theoretical and Mathematical Sciences Program (iTHEMS), Wako 351-0198, Japan and Department of Physics, Graduate School of Science, The University of Tokyo, Tokyo 113-0033, Japan

Tomohiro Oishi (大石知広)[†]
Yukawa Institute for Theoretical Physics, Kyoto University, Kyoto 606-8502, Japan

Hiroyuki Sagawa (佐川弘幸)[‡]
Center for Mathematics and Physics, University of Aizu, Aizu-Wakamatsu 965-8560, Japan and RIKEN Nishina Center, Wako 351-0198, Japan

Zhiheng Wang (王之恒)[§]
School of Nuclear Science and Technology, Lanzhou University, Lanzhou 730000, China and Frontiers Science Center for Rare Isotopes, Lanzhou University, Lanzhou 730000, China

(Received 27 October 2022; accepted 27 April 2023; published 18 May 2023)

Isotope dependences of charge radii, i.e., isotope shifts, calculated by the Skyrme Hartree-Fock, the relativistic mean-field, and the relativistic Hartree-Fock calculations are compared against the experimental data of magic and semimagic nuclei. It is found that the tensor interaction plays a role in reproducing the "kink" behavior, irregularity of isotope shifts at the neutron magic number, in the relativistic Hartree-Fock approach. With several Skyrme models, it is found that the kink behavior can be reproduced with the spin-orbit interaction having nonzero isovector channel. The single-particle orbitals near the Fermi energy are crucial to determine the kink size. The effects of the symmetry energy and the pairing interaction are also discussed in relation to the kink behavior.

DOI: 10.1103/PhysRevC.107.054307

I. INTRODUCTION

Charge radii of atomic nuclei $R_{\rm ch}$ are one of the important properties of atomic nuclei, which can be measured precisely via the electron scattering [1,2] and the laser spectroscopy [3,4]. The isotope dependence of $R_{\rm ch}$, i.e., the isotope shift, has been discussed for a long time theoretically and experimentally. The slope of $R_{\rm ch}$ as a function of the neutron number N is known to change at the neutron magic number, which is called the "kink" behavior. It was discussed in Ref. [5] that the kink behavior of Pb isotopes can be reproduced if the strengths of isoscalar and isovector spin-orbit interaction in the Skyrme energy density functional (EDF) is properly adjusted. Recently, it was discussed using the M3Y-P6a interaction that the kink behavior is also reproduced by the three-body spin-orbit interaction [6]. The kink behavior was also discussed by using the relativistic mean-field calculation in Ref. [7], in which the importance of the occupation probabilities above the shell gap was pointed out. The kink behavior of mercury isotopes was also discussed recently in Refs. [8–10].

The aim of this paper is to discuss whether the kink behavior is reproduced even in the "normal" treatment, i.e., mean-field models with a widely used functional and a standard contact pairing interaction, without any additional terms or effects. In this paper, we compare $R_{\rm ch}$ of Sn and Pb isotopes obtained by the nonrelativistic Skyrme Hartree-Fock (SHF) [11], the relativistic mean-field (RMF) [12,13], and the relativistic Hartree-Fock (RHF) [14,15] calculations. This comparison enables us to discuss the kink behavior from two perspectives on the spin-orbit splitting. In the nonrelativistic Skyrme energy density functional calculation, the spin-orbit splitting is phenomenologically determined by the parameters, the isoscalar spin-orbit strength W_0, and the isovector one W_0'. On the other side, in the relativistic mean-field calculations, where the single-particle state is described with the Dirac equation obtained self-consistently from the relativistic EDF, the spin-orbit splitting is induced by the relativistic effect without introducing any additional parameter. In the RHF model, the tensor interaction can also be included when the Fock terms are explicitly considered. Using such comparisons, we will be able to find out how much the tensor interaction, and its contribution to the spin-orbit field, is important to reproduce the kink behavior. In addition, we will

[*]tnaito@ribf.riken.jp
[†]Current address: RIKEN Nishina Center, Wako 351-0198, Japan; tomohiro.oishi@yukawa.kyoto-u.ac.jp
[‡]sagawa@ribf.riken.jp
[§]wangzhh2013@lzu.edu.cn

also study a correlation between the symmetry energy of the nuclear equation of state and the kink behavior.

This paper is organized as follows. In Sec. II, the theoretical framework of this paper will be given. In Sec. III B, the calculation results of Sn isotopes will be presented, where the detailed discussion of the occurrence mechanism of the kink behaviors will be given. In Sec. III C, the calculation results of Pb isotopes will be shown, where the detailed discussion will be mainly referred to in Sec. III B. In Sec. III D, effects of parameters of the nuclear equation of state on the kink behavior will be shown. In Sec. III E, effects of the pairing strength and interaction will be discussed. In Sec. III F, the calculation results of Ca isotopes will be given, where it will be found that beyond-mean-field effects are indispensable to reproduce the isotope dependence of $R_{\rm ch}$ of Ca isotopes. In Sec. IV, this paper will be summarized.

II. THEORETICAL FRAMEWORK

The methods used in this paper can be classified into two classes: the nonrelativistic framework and the relativistic one. We use the SHF calculation for the former and the RMF and RHF calculations for the latter.

In the SHF calculation, the following Skyrme EDFs are used: SAMi [16], SGII [17], SLy4 [18], SLy5 [18], SkM* [19], HFB9 [20], UNEDF0 [21], UNEDF1 [22], and UNEDF2 [23]. In addition, the Skyrme EDF with the tensor interaction "SAMi-T" [24] is used, in which all the parameters, including the tensor interaction, were simultaneously optimized to fit a set of experimental data. To see the effect of the tensor interaction, the SAMi-T EDF without the tensor interaction is also used being referred to as "SAMi-noT". A variety of SAMi EDFs with the different value for the effective mass, the symmetry energy, and the nuclear incompressibility, called "SAMi-m" [25], "SAMi-J" [25], and "SAMi-K" [26] families, respectively, are also adopted in order to see whether properties of nuclear equation of state (EoS) affect the kink behavior. The parameters of all these SAMi EDFs are optimized for the same set of experimental data. The pairing interaction is taken into account by using the Hartree-Fock-Bogoliubov calculation with the volume-type pairing interaction [27]

$$V_{\rm pair}(\boldsymbol{r}_1, \boldsymbol{r}_2) = -V_0 \delta(\boldsymbol{r}_1 - \boldsymbol{r}_2) \tag{1}$$

with the cutoff energy of 60 MeV, whose strength is determined to reproduce the neutron pairing gap of ^{120}Sn as $\Delta_n = 1.4$ MeV. The strengths for different EDFs are shown in Table I. All the calculations are performed by using the harmonic oscillator basis [28] under the assumption of spherically symmetric shape. Since all nuclei studied are magic or semimagic ones, this assumption on the shape is reasonable.

In the RMF calculation, the Fock term is neglected and correspondingly the EDF is optimized in order to reproduce the reference data. The RHF calculation, on the other hand, takes the Fock term into account and the parameters of the relativistic EDF are optimized with the reference data as the RMF model. In the RMF calculation, the DD-PC1 [29], DD-ME2 [30], PKDD [31], and DD-LZ1 [32] EDFs are used, while in the RHF calculation, the PKO1 [33], PKO2 [33], PKO3 [33], PKA1 [34], and the modified version of the PKO1, which will be referred to as the PKO1* [35], are used. The pairing correlation is considered by using the Bardeen-Cooper-Schrieffer (BCS) theory, the Tian-Ma-Ring (TMR)-type pairing interaction [36] is used for DD-PC1 and DD-ME2, and the surface-type pairing interaction [37] with the pairing strength of 500 MeV fm^3 is used for DD-ME2, PKDD, DD-LZ1, PKO1, PKO2, PKO3, PKO1*, and PKA1. All the calculations are performed assuming the spherically symmetric shape for the harmonic oscillator or Woods-Saxon basis.

In this paper, the same pairing strengths are used for both the proton-proton and the neutron-neutron channels. We confirmed that the results hardly change even if the Coulomb antipairing effect [38] is considered.

After the proton and neutron root-mean-square radii, R_p and R_n, are obtained by using SHF, RMF, and RHF, the charge radius $R_{\rm ch}$ is calculated by using a formula for the finite-size

TABLE I. Adopted pairing strengths for Skyrme EDFs in this study. The volume-type pairing interaction is used and the energy cutoff is 60 MeV.

Skyrme EDF	V_0 (MeV fm^3)
SLy4	194.2
SLy5	188.2
HFB9	164.4
SkM*	156.2
SGII	169.8
UNEDF0	127.6
UNEDF1	138.4
UNEDF2	150.0
SAMi	213.7
SAMi-noT	216.4
SAMi-T	225.5
SAMi-K230	213.8
SAMi-K235	206.9
SAMi-K240	201.2
SAMi-K245	209.6
SAMi-K250	208.2
SAMi-K255	206.9
SAMi-K260	205.5
SAMi-m60	227.6
SAMi-m65	215.2
SAMi-m70	203.9
SAMi-m75	194.3
SAMi-m80	185.4
SAMi-m85	177.3
SAMi-J27	205.0
SAMi-J28	208.3
SAMi-J29	212.0
SAMi-J30	215.1
SAMi-J31	217.6
SAMi-J32	219.3
SAMi-J33	220.2
SAMi-J34	220.4
SAMi-J35	220.2

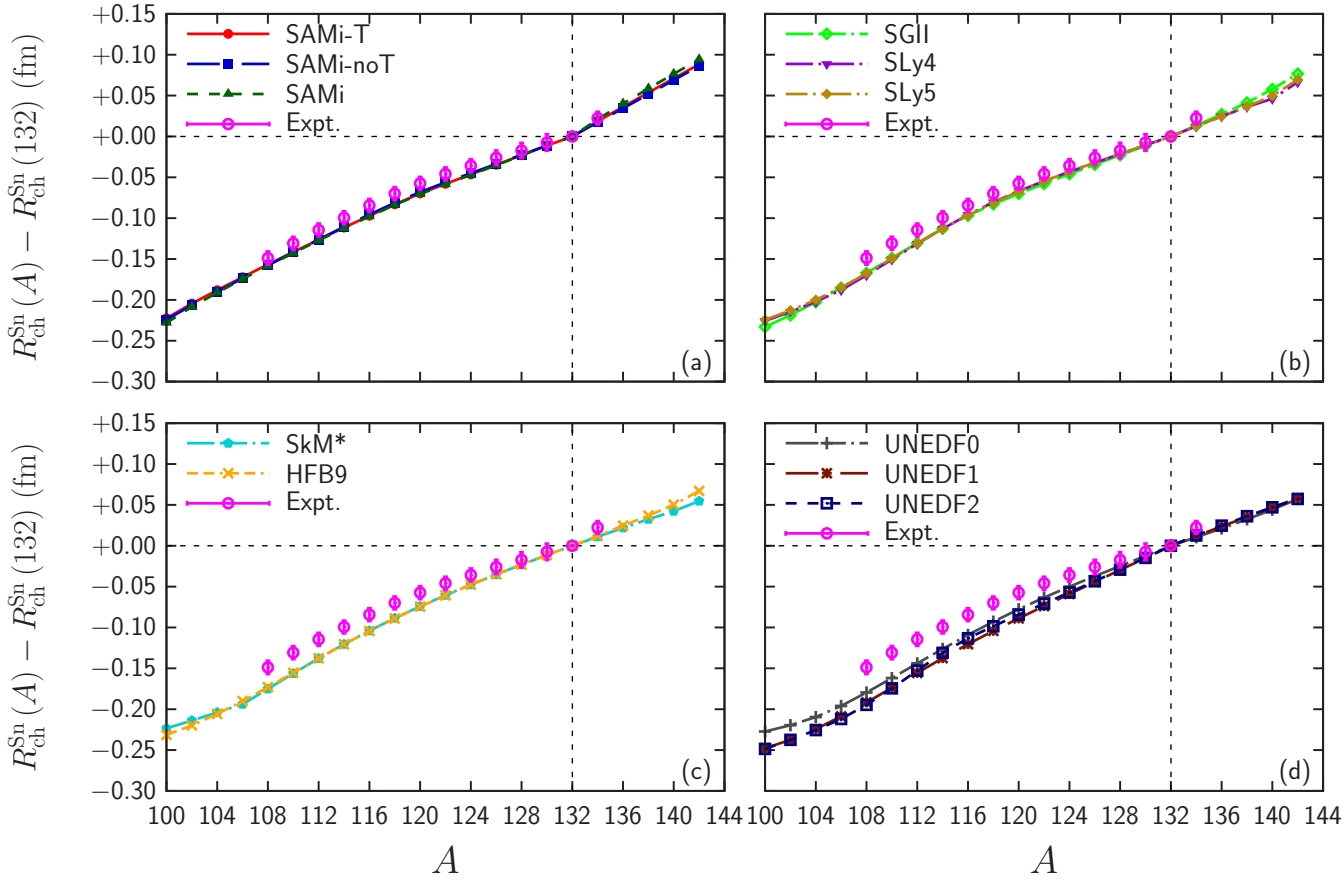

FIG. 1. Difference of root-mean-square charge radii between ^{A}Sn and ^{132}Sn, $R_{\rm ch}^{\rm Sn}(A) - R_{\rm ch}^{\rm Sn}(132)$, as a function of A calculated by using nonrelativistic EDFs. For comparison, experimental data [3,41] are also plotted.

effect of nucleons,

$$R_{\rm ch}^2 = R_p^2 + r_{{\rm E}p}^2 + \frac{N}{Z} r_{{\rm E}n}^2 + \langle r^2 \rangle_{{\rm SO}p} + \frac{N}{Z} \langle r^2 \rangle_{{\rm SO}n}, \qquad (2)$$

where $r_{{\rm E}p} = 0.8409$ fm is the single proton radius and $r_{{\rm E}n}^2 = -0.1161$ fm^2 is the single neutron mean-square radius [39]. The spin-orbit contributions $\langle r^2 \rangle_{{\rm SO}p}$ and $\langle r^2 \rangle_{{\rm SO}n}$ obtained in Ref. [40] are calculated with the nucleon magnetic moments $\kappa_p = 1.793$ and $\kappa_n = -1.913$ [39]. The importance of the spin-orbit contribution will be discussed in the Appendix.

III. CALCULATED RESULTS

In this section, the "kink" behaviors of Sn and Pb isotopes will be presented. The detailed mechanism will be discussed by using Sn isotopes since ^{132}Sn or its neighbor nuclei are not used for the fitting criteria of the EDFs, and thus, it is expected that the results may reflect properties of the EDFs better. Then, the effects of some parameters of the nuclear equation of state on the kink properties will also be discussed, introducing the symmetry energy J, the nuclear incompressibility K_∞, and the effective mass m^*. Dependences of the pairing strength and interaction on the kink behavior will also be discussed. At last, results of Ca isotopes will be presented.

A. Mass-number A dependence of charge radii in Sn and Pb isotopes

The mass-number A dependence of the difference between the root-mean-square charge radius of ^{A}Sn and that of ^{132}Sn, $R_{\rm ch}^{\rm Sn}(A) - R_{\rm ch}^{\rm Sn}(132)$, calculated in nonrelativistic (SHF) and relativistic (RMF and RHF) EDFs are shown in Figs. 1 and 2, respectively. For comparison, experimental data [3,41] are also plotted. Results for Pb isotopes, $R_{\rm ch}^{\rm Pb}(A) - R_{\rm ch}^{\rm Pb}(208)$, are shown in Figs. 3 and 4 as well.

It can be seen that most EDFs reproduce well the A dependence of $R_{\rm ch}$ of stable nuclei of Sn isotopes ($62 \leqslant N \leqslant 74$) except UNEDF2, PKA1, and DD-LZ1. In Figs. 3 and 4, most EDFs reproduce well the A dependence of Pb isotopes below the magic number $N = 126$, although the UNEDF series underestimate $R_{\rm ch}^{\rm Pb}(A) - R_{\rm ch}^{\rm Pb}(208)$ slightly, and the DD-LZ1 EDF overestimates it slightly. Behavior above the magic numbers is the main topic in this paper, and will be presented later.

B. Sn isotopes

1. Systematic behavior

Hereinafter, we focus only on the kink behavior. To discuss the size of kink quantitatively, we define the indicator of kink

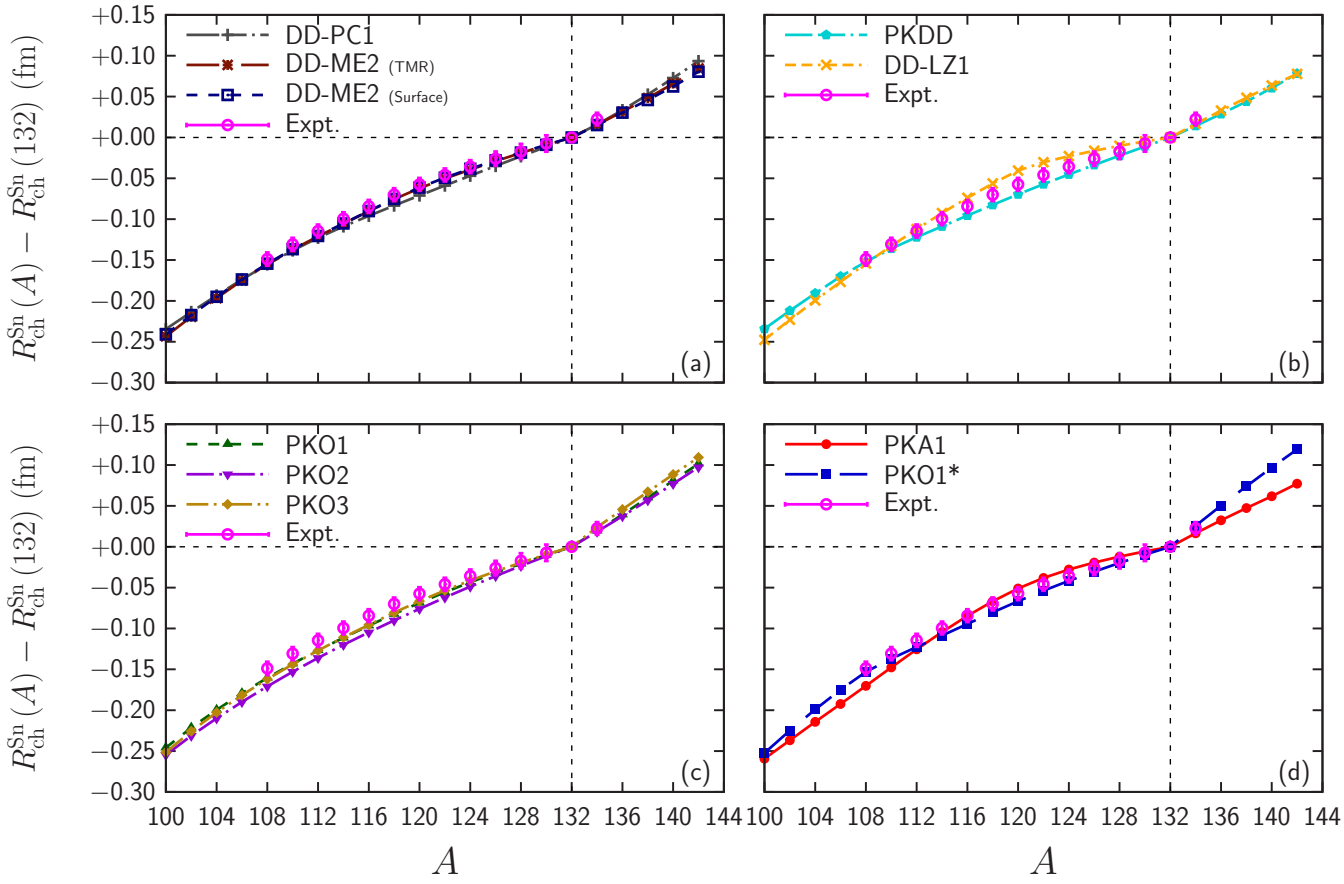

FIG. 2. Same as Fig. 1, but by using relativistic EDFs.

size $\Delta^2 R_{\rm ch}^Z$ as

$$\Delta^2 R_{\rm ch}^Z = \Delta R_{\rm ch}^Z(A_{\rm magic}+2) - \Delta R_{\rm ch}^Z(A_{\rm magic}) = R_{\rm ch}^Z(A_{\rm magic}+2) - 2R_{\rm ch}^Z(A_{\rm magic}) + R_{\rm ch}^Z(A_{\rm magic}-2), \quad (3)$$

where $A_{\rm magic}$ is the mass number corresponding to doubly magic nuclei, i.e., $A_{\rm magic} = 48$ for $Z = 20$ (Ca), $A_{\rm magic} = 132$ for $Z = 50$ (Sn), and $A_{\rm magic} = 208$ for $Z = 82$ (Pb) and

$$\Delta R_{\rm ch}^Z(A) = R_{\rm ch}^Z(A) - R_{\rm ch}^Z(A-2). \quad (4)$$

This indicator corresponds to the discretized second derivative of $R_{\rm ch}$ at $A = A_{\rm magic}$, which is related to the curvature of the graph in the continuum limit. The larger value corresponds to the larger (stronger) kink. The kink indicators for Sn isotopes are summarized in Tables II and III for Skyrme EDFs and relativistic EDFs, respectively. From Tables II and III, one general tendency is found: The results of relativistic (RMF and RHF) models give stronger kinks than the nonrelativistic (SHF) ones, while the EDF dependence among the members of each model is large. In the nonrelativistic SHF, UNEDF series somehow yields a smaller kink commonly than other EDFs. In the relativistic cases, the RHF calculations give larger kinks than those of the RMF ones, except the DD-LZ1 EDF.

One can find that the SHF calculations, except SAMi, SAMi-noT, and SAMi-T, provide a smaller kink than those of the relativistic (RMF and RHF) ones. We found that, in general, the RHF calculations provide the larger kink than the RMF ones. This can be understood as follows: As will be discussed, the spin-orbit interaction is important for the kink behavior [6]. The spin-orbit mean field appears from both the relativistic effect and the tensor interaction in RHF calculation, while only from the former in RMF calculation; hence,

TABLE II. Kink indicator $\Delta^2 R_{\rm ch}^{\rm Sn}$ for Sn calculated by nonrelativistic EDFs. The charge radius differences $\Delta R_{\rm ch}^{\rm Sn}(132)$ and $\Delta R_{\rm ch}^{\rm Sn}(134)$ are also listed. All values are given in units of 10^{-3} fm.

EDF	$\Delta R_{\rm ch}^{\rm Sn}(132)$	$\Delta R_{\rm ch}^{\rm Sn}(134)$	$\Delta^2 R_{\rm ch}^{\rm Sn}$
UNEDF1	+14.913	+11.886	−3.027
UNEDF2	+14.850	+12.571	−2.279
UNEDF0	+12.495	+10.479	−2.016
SkM*	+11.456	+11.027	−0.429
HFB9	+11.302	+12.222	+0.920
SLy4	+10.665	+12.449	+1.784
SLy5	+10.568	+12.363	+1.795
SGII	+11.436	+13.446	+2.010
SAMi-noT	+11.101	+17.318	+6.217
SAMi-T	+11.196	+18.507	+7.311
SAMi	+11.229	+21.092	+9.863
Expt.	+7.4	+22.4	+15.0

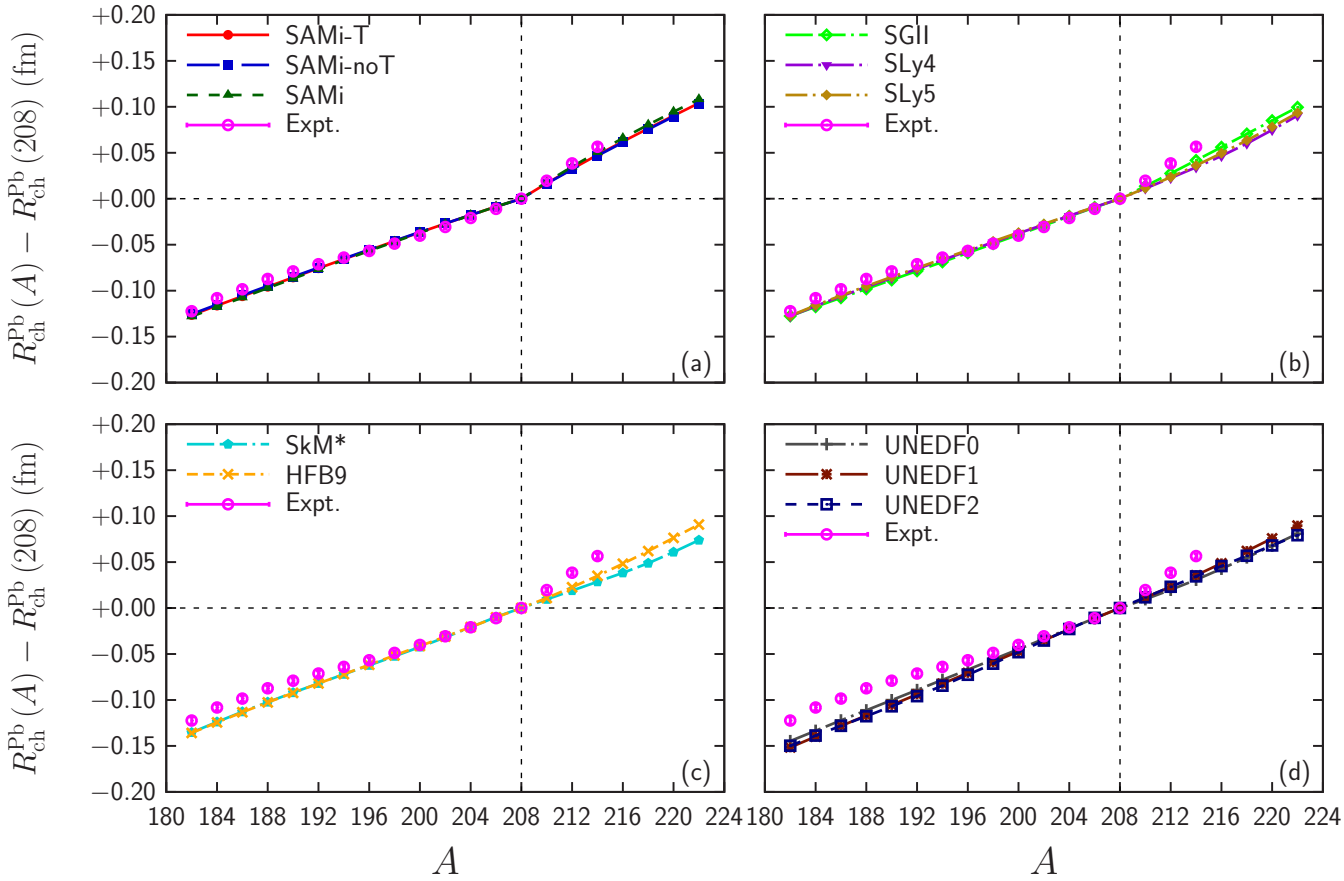

FIG. 3. Same as Fig. 1, but for Pb isotopes with the reference point at ^{208}Pb, $R_{\rm ch}^{\rm Pb}(A) - R_{\rm ch}^{\rm Pb}(208)$.

the origin of the spin-orbit interaction of the RMF calculation is different compared to that of the RHF calculation. The spin-orbit interaction in the Skyrme calculation is introduced phenomenologically as the W_0 and W_0' terms without any density dependence. Discussion of the density dependence of the spin-orbit interaction in the Skyrme interaction can be found in Refs. [42–45].

Among Skyrme EDFs, the UNEDF series provide the "antikink"; the SkM* and HFB9 do not provide visible kink; and the SLy4, SLy5, and SGII give the kink, but the magnitude is smaller than the experimental one. The SAMi, SAMi-noT, and SAMi-T provide the kink larger than the other Skyrme EDF. The SAMi EDF is constructed to give the better description of spin-isospin properties, such as Gamow-Teller resonances [16], where the strength of the spin-orbit interaction stems from the spin-isospin transitions involving the spin-orbit partner levels. Hence, we conjecture that the modeling with respect to the spin-orbit splitting is essential to describe the kink better. Note that the SGII is also constructed towards Gamow-Teller resonances [17], but it does not give the kink as large as the SAMi. It is worthwhile to mention that, in Pb isotopes, SAMi series and SGII give stronger kinks than other Skyrme EDFs as will be shown later.

TABLE III. Same as Table II, but calculated by relativistic EDFs.

EDF	$\Delta R_{\rm ch}^{\rm Sn}(132)$	$\Delta R_{\rm ch}^{\rm Sn}(134)$	$\Delta^2 R_{\rm ch}^{\rm Sn}$
PKDD	+11.088	+14.166	+3.078
DD-PC1	+11.411	+15.862	+4.451
DD-ME2 (Surface)	+9.055	+15.159	+6.104
DD-ME2 (TMR)	+9.290	+15.587	+6.297
PKO2	+11.424	+18.474	+7.050
PKO1	+10.172	+19.566	+9.394
PKA1	+5.691	+16.512	+10.821
DD-LZ1	+4.836	+16.631	+11.795
PKO3	+9.455	+23.896	+14.441
PKO1*	+9.629	+25.748	+16.119
Expt.	+7.4	+22.4	+15.0

The SkI4 EDF also gives the kink behavior of Pb isotopes [5]. References [5,46] claim that the introduction of the isoscalar and isovector spin-orbit interactions, W_0 and W_0', is essential, while the standard Skyrme EDFs have only the isoscalar term ($W_0 = W_0'$). Among better EDFs to describe the kink behavior, the two strengths are identical, $W_0 = W_0'$ in the SGII EDF; in the SkI4 EDF, the isoscalar and isovector spin-orbit interactions have opposite signs, namely, $W_0' < 0 < W_0$ and $|W_0'| < W_0$; in the SAMi EDF, the isoscalar and isovector spin-orbit interactions are of the same direction, but the strengths are different, $0 < W_0' < W_0$. Since their strengths and signs of W_0 and W_0' are different and rather arbitrary, it is not possible at the moment which combination of W_0 and W_0' values are the best for the kink behavior. It should be noted

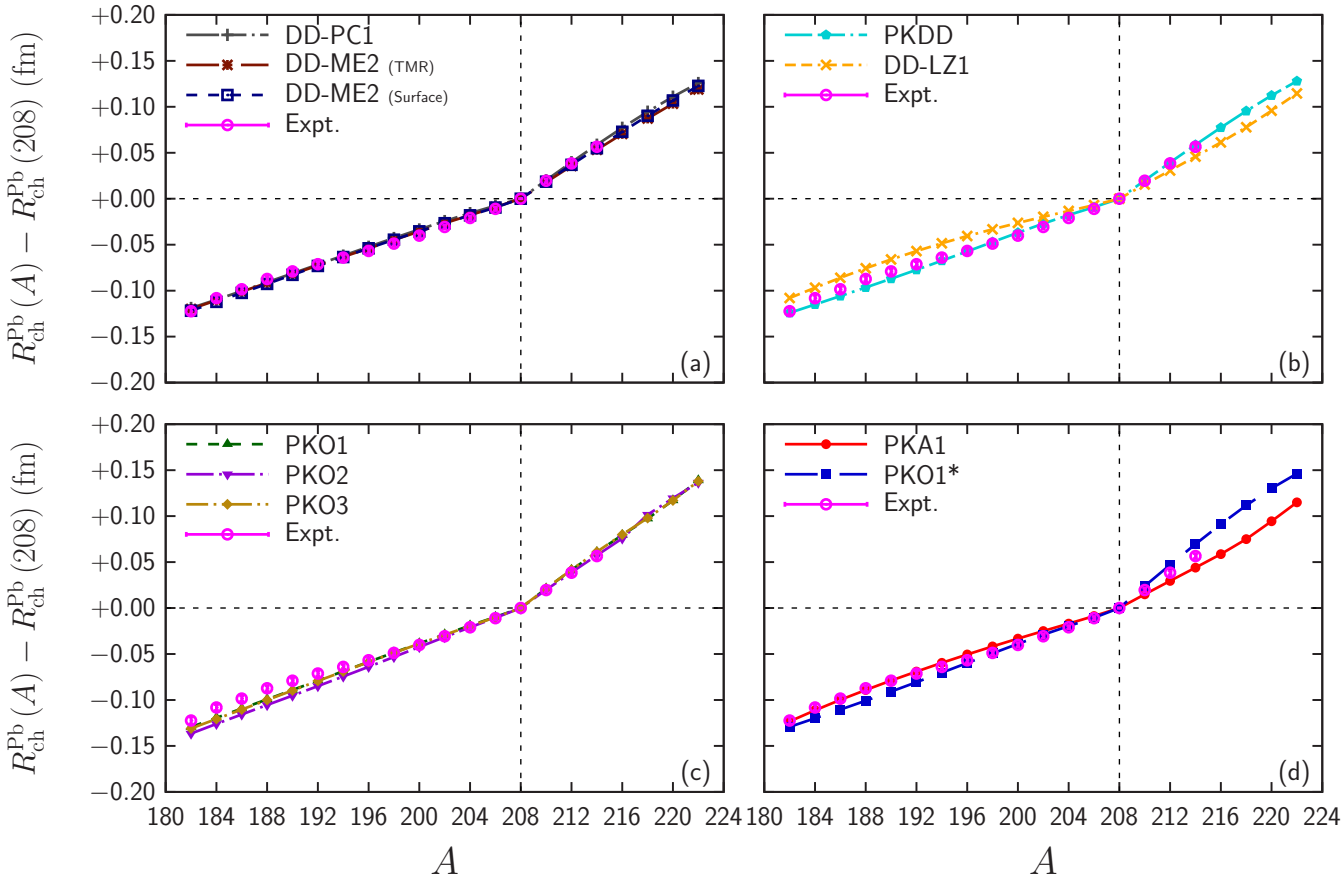

FIG. 4. Same as Fig. 2, but for Pb isotopes with the reference point at ^{208}Pb.

that the detailed discussion of W_0 and W_0' can be found in Refs. [44,47–50].

Comparing the results of the SAMi-T and the SAMi-noT EDFs, one can see how the Skyrme tensor interaction affects the kink behavior. Although the SAMi-T EDF gives the stronger kink than the SAMi-noT EDF and the Skyrme tensor interaction makes the slope above the shell gap steeper, its effect is not so significant. Moreover, the shell structure, which will be discussed later, is not changed much by the tensor terms. Therefore, the Skyrme tensor interaction introduces additional spin-orbit terms in the mean field, but its effect is not so strong as far as SAMi-T is concerned. This is because the effect of the tensor interaction may be already included in the original spin-orbit interaction during the fitting procedure.

Next, we shall focus on the relativistic calculation. Except for the DD-LZ1 EDF, the RMF calculations give a smaller kink than the RHF calculations, while the DD-LZ1 EDF gives a comparable size of kink with those of the RHF calculations. Among the RHF calculations, the kink size of PKO2 is the weakest and PKO3 and PKO1* give appreciable kinks. It should be noted that although the PKA1 and the DD-LZ1 give the strong kink, their slopes above $N = 82$ are not so steep; the reason why their kink sizes are large is that the slopes below $N = 82$ are loose. Indeed, the slope above $N = 82$ of the PKA1 is the smallest among the RHF calculations, while the slope above $N = 82$ of the DD-LZ1 is still largest among the RMF calculations. To check the pairing model dependence, two results of DD-ME2 with different pairing interactions, denoted by "DD-ME2 (TMR)" and "DD-ME2 (Surface)", are shown in Fig. 2, where the former and the latter, respectively, correspond to the Tian-Ma-Ring (TMR) type [36] and the surface-type pairing interactions. One can easily find that these two pairing interactions give almost the same kink size.

The PKO1, PKO2, PKO3, PKO1*, and PKA1 basically start from the same Lagrangian, while the number of mesons and their meson-nucleon coupling constants are different. The mesons considered in these EDFs are summarized in Table IV. This suggests that π-PV, ρ-T, and ρ-VT couplings, which gives the tensor interaction, are important to reproduce the kink behavior. According to Ref. [35], the strength of the tensor interaction of PKO2 is weakest and that of PKO1* is the strongest; that of PKO3 is the second strongest, and those of PKA1 and PKO1 are marginal. Strengths of the tensor interaction of these interactions are consistent with the kink size: the stronger the tensor interaction the larger the kink size. Therefore, the tensor interaction or its outcomes, such as spin-orbit mean field, and shell structure, are important to reproduce the kink behavior. This is in contrast to the nonrelativistic case.

The DD-LZ1 EDF is constructed with the guidance of pseudospin symmetry restoration [51] and, as a result, shell

TABLE IV. Mesons considered in PKDD, DD-ME2, DD-LZ1, PKO1, PKO2, PKO3, PKO1*, and PKA1 EDFs. All the couplings are density dependent.

EDF	π-PV	ρ-V	ρ-T	ρ-VT	ω-V	σ-S
PKDD	No	Yes	No	No	Yes	Yes
DD-ME2	No	Yes	No	No	Yes	Yes
DD-LZ1	No	Yes	No	No	Yes	Yes
PKA1	Yes	Yes	Yes	Yes	Yes	Yes
PKO1	Yes	Yes	No	No	Yes	Yes
PKO2	No	Yes	No	No	Yes	Yes
PKO3	Yes	Yes	No	No	Yes	Yes
PKO1*	Yes	Yes	No	No	Yes	Yes

evolution was described better than other popular RMF EDFs [32]. It is constructed without an ansatz of density dependences of some meson couplings and fitted to ^{218}U, which is related to the subshell closure of $Z = 92$. The pseudospin symmetry is strongly related to the spin-orbit splitting [52]. This fact is in agreement with our conjecture that the spin-orbit splitting is important to reproduce the kink size.

2. *Single-particle energies*

To understand the kink behaviors better, the single-particle spectra of neutrons of ^{132}Sn are shown in Figs. 5 and 6. The magenta dotted line indicates the $N = 82$ shell gap. All the calculations show that the $2f_{7/2}$ orbital is just above the $N = 82$ shell gap, but above the $2f_{7/2}$ orbital, the order of valence-neutron orbitals noticeably depends on the EDF utilized. Especially, the $1h_{9/2}$ orbital appears just above the $2f_{7/2}$ orbital in SAMi, SAMi-noT, SAMi-T, DD-PC1, PKO3, and PKO1* calculations, in which the kink is strong as listed in Tables II and III. Therefore, the order of the single-particle orbitals above the shell gap will play an important role as mentioned in Ref. [7]. To understand this mechanism more clearly, the occupation probabilities of the single-particle orbitals just above the shell gap of ^{134}Sn are plotted in Figs. 7 and 8. Here, the occupation probability, which ranges between 0 and 1, is defined by the occupation number divided by the maximum occupation number. The correlation between the occupation probability of the $1h_{9/2}$ orbital and the slope above the $N = 82$ gap $[\Delta R^{\rm Sn}_{\rm ch}(134)]$ is plotted in Fig. 9. It is easily seen that, in general, the larger occupancy of the $1h_{9/2}$ orbital gives the steeper slope, and accordingly the larger kink, for instance, in SAMi, SAMi-noT, SAMi-T, and the PKO series. One possible explanation on this kink-evolution effect of $1h_{9/2}$ is as follows: the $1h_{9/2}$ orbital does not have the nodal structure, while the $2f_{7/2}$ one has a node. The former has larger overlap with the protons and thus it extends the charge radius due to the proton-neutron attractive interaction, as discussed in Ref. [7]. Thus, when the two valence neutrons above the $N = 82$ shell occupy this orbital, the mean radial distribution is suddenly enhanced. The DD-LZ1 again shows an exceptional behavior: Its kink size is noticeably strong, although the occupation probability of the $1h_{9/2}$ orbital is small. A similar result is obtained with PKA1. For the large size of the kink of DD-LZ1 and PKA1, an alternative hint is possibly given by considering the single-particle levels. In Fig. 6, the energies of $1h_{9/2}$ obtained from the DD-LZ1 and PKA1 are located higher than the other relativistic EDFs' results, and thus, their radial distributions can become wider. Even if its occupation probability is small, a finite mixing of this $1h_{9/2}$ component can enhance the sudden change of radial distributions between ^{132}Sn and ^{134}Sn, as well as the size of kink.

It is also shown that the occupation probability of the $3p_{3/2}$ orbital is much larger than the $1h_{9/2}$ orbital in the UNEDF0,

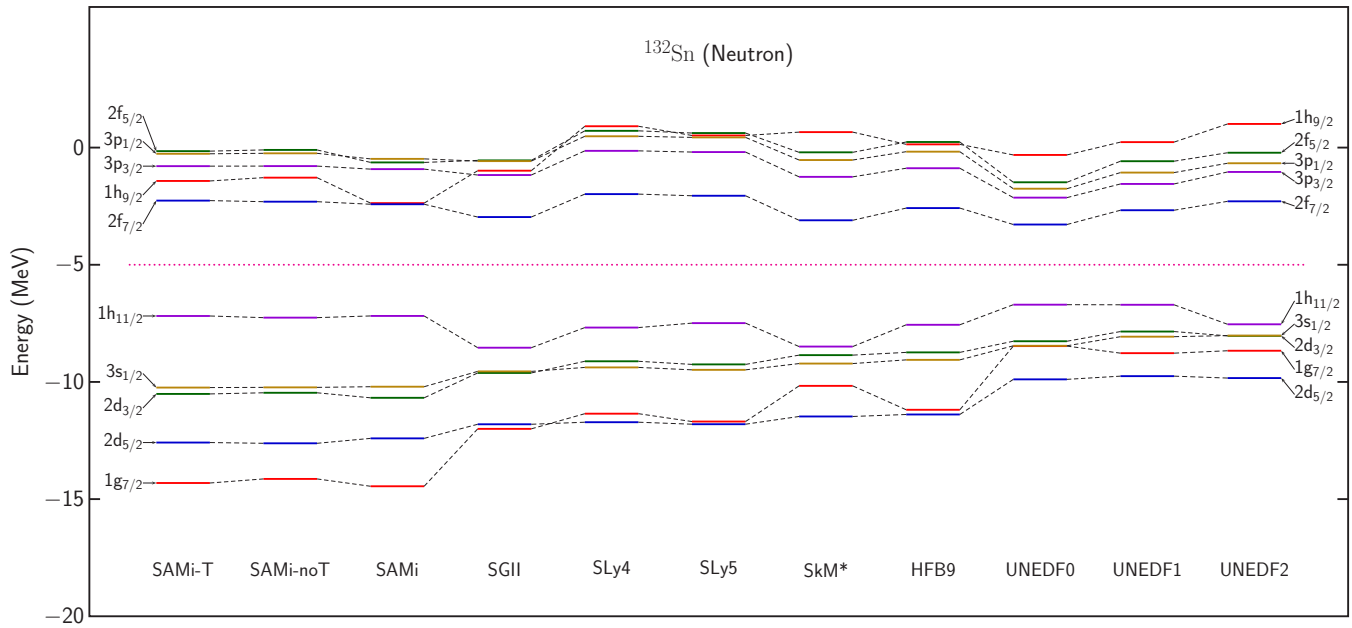

FIG. 5. Single-particle spectra of ^{132}Sn calculated in nonrelativistic EDFs.

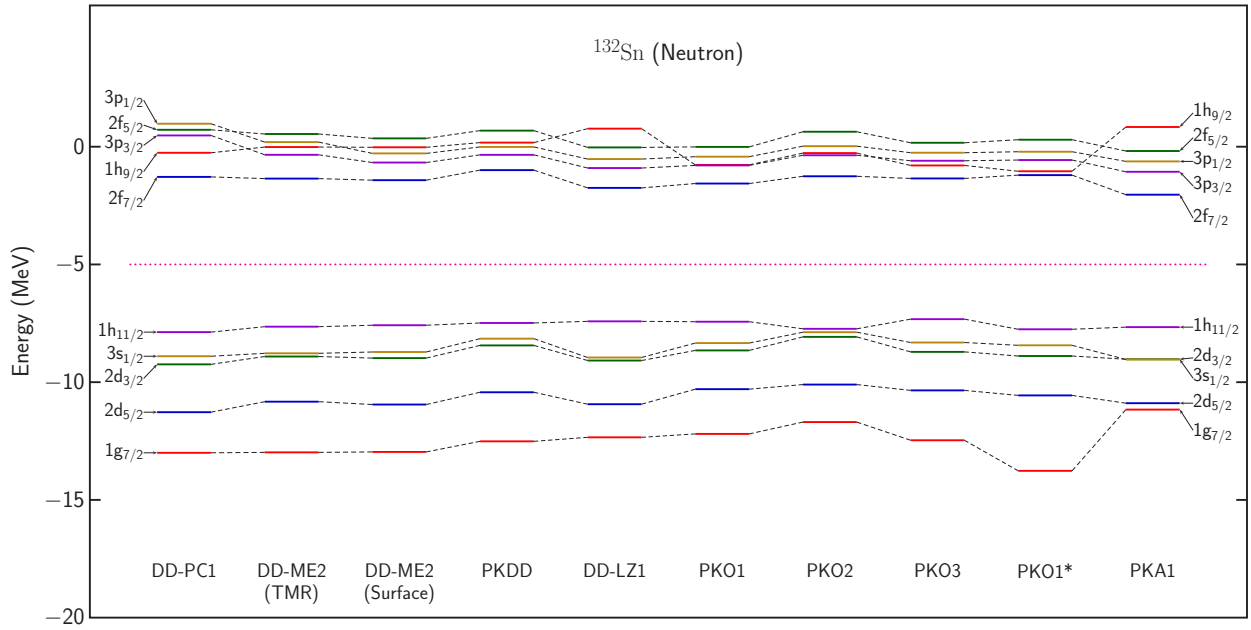

FIG. 6. Same as Fig. 5, but by using relativistic EDFs.

UNEDF1, and UNEDF2, which show the "antikink" behavior at $N = 82$. These antikinks also originate from the steep slope below $N = 82$ and the moderate slopes above $N = 82$.

The occupation probabilities of the orbitals near the Fermi level depend on the single-particle energies. The occupation probabilities affect the kink size, as well as the spin-orbit interaction. In order to discuss the effect of the single-particle energies, the spin-orbit interaction should be *effectively* switched off. To this end, the average energy of the spin-orbit partners $\overline{\varepsilon}$ is considered here. This $\overline{\varepsilon}$ is not affected by the spin-orbit potential but by the central potential. The spin-orbit interaction for the orbital with the orbital angular momentum l is proportional to l for $j = l + 1/2$ orbitals and $-(l + 1)$ for $j = l - 1/2$ orbitals. Therefore, the *averaged* single-particle energy for the l orbital is defined by

$$\overline{\varepsilon} = \frac{l}{2l+1}\varepsilon_{<} + \frac{l+1}{2l+1}\varepsilon_{>}, \tag{5}$$

where $\varepsilon_{<}$ and $\varepsilon_{>}$ are the single-particle energies for $j = l - 1/2$ and $l + 1/2$ orbitals, respectively. Figures 10 and 11 show the correlation between the averaged single-particle energies $\overline{\varepsilon}$ of the $1h$ and $2f$ orbitals in ^{134}Sn and the kink size $\Delta^2 R_{\rm ch}$ in the nonrelativistic and relativistic schemes, respectively. There is a weak correlation between $\overline{\varepsilon}$ of the $1h$ orbital and the kink size. As $\overline{\varepsilon}$ of the $1h$ orbital is small, the $1h_{9/2}$ orbital becomes lower and accordingly the occupation probability of the $1h_{9/2}$ orbital becomes larger. The occupation probability of the $1h_{9/2}$ orbitals is correlated to the kink size as discussed above. We also found that there is no obvious correlation between $\overline{\varepsilon}$ of the $2f$ orbital and the kink size. In Figs. 12 and 13, the correlation between the difference between two average energies, $\overline{\varepsilon}_{2f} - \overline{\varepsilon}_{1h}$, and the kink size is shown. We found that, in contrast to the case of bare $\overline{\varepsilon}$, there is a clear correlation between $\overline{\varepsilon}_{2f} - \overline{\varepsilon}_{1h}$ and $\Delta^2 R_{\rm ch}^{\rm Sn}$ in the nonrelativistic calculation. We also found that if the pion contribution is included in the RHF calculation; the smaller

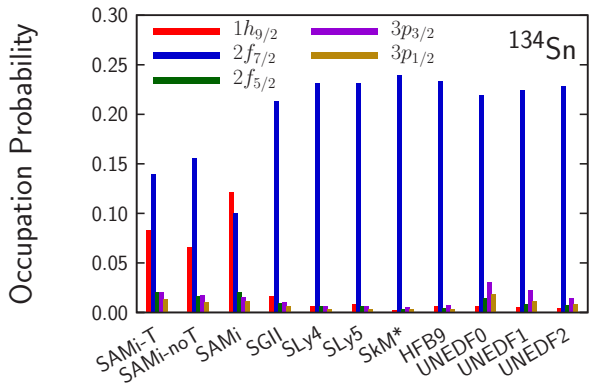

FIG. 7. Occupation probability of orbitals above the $N = 82$ shell gap for ^{134}Sn calculated by using nonrelativistic EDFs.

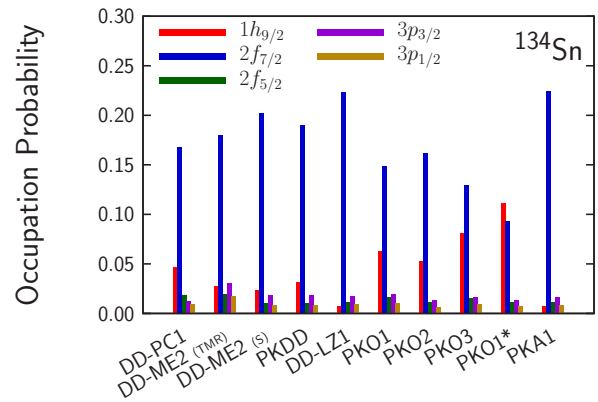

FIG. 8. Same as Fig. 7, but by using relativistic EDFs.

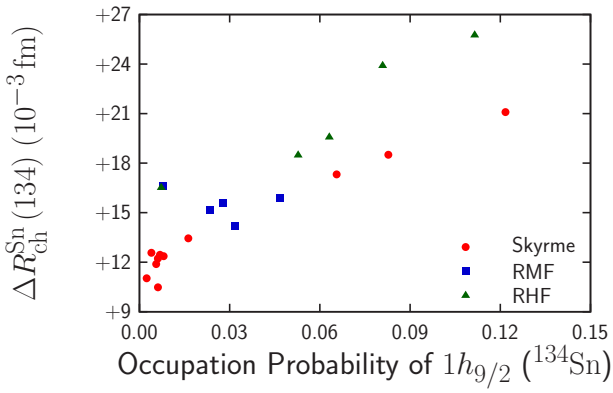

FIG. 9. Correlation between occupation probability of $1f_{9/2}$ orbital of ^{134}Sn and kink size at $N = 82$.

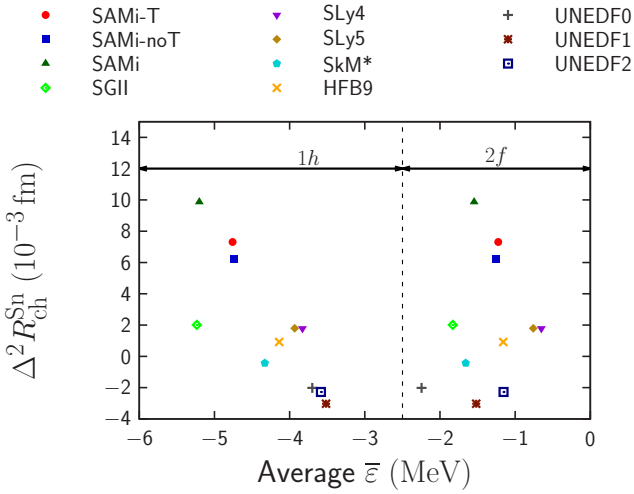

FIG. 10. Correlations between the averaged single-particle energies of $1h$ and $2f$ orbitals of ^{134}Sn and the kink size calculated by using nonrelativistic EDFs.

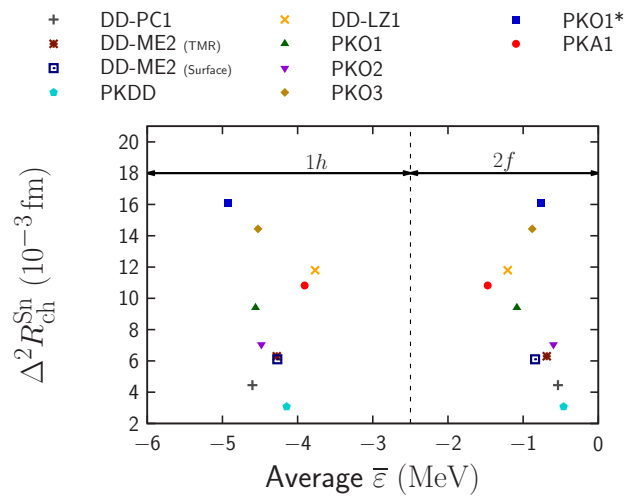

FIG. 11. Same as Fig. 10, but by using relativistic EDFs.

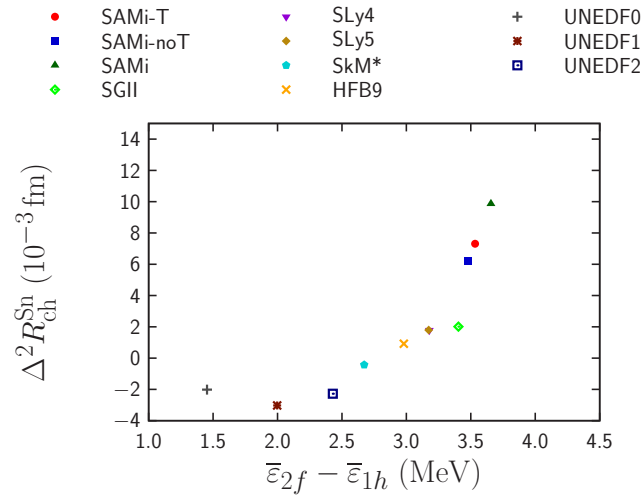

FIG. 12. Correlations between the difference between the averaged single-particle energies of $1h$ and $2f$ orbitals of ^{134}Sn and the kink size calculated by using nonrelativistic EDFs.

$\overline{\varepsilon}_{2f} - \overline{\varepsilon}_{1h}$ gives the smaller $\Delta^2 R_{\rm ch}^{\rm Sn}$, while other correlation is not obvious in the relativistic calculation. Note that similar analysis for the band termination was done in Ref. [53].

By summarizing the above discussions, to evolve the kink behavior of $R_{\rm ch}$ at $N = 82$, the occupation probability of the $1h_{9/2}$ orbital, which is located above the $2f_{7/2}$ orbital, must be large enough. In order to lower the $1h_{9/2}$ orbital, the spin-orbit interaction should not be too strong. Otherwise, the $1h_{9/2}$ level becomes higher than the $2f_{7/2}$ one in energy and also the $3p_{3/2}$ energy can be too low, which is the origin of the antikink. The spin-orbit gaps of the $1h$ orbitals calculated by the UNDEF0, UNEDF1, and UNEDF2 are almost the same as the other Skyrme EDFs except for the SAMi series. However, the occupation probability of the $1h_{9/2}$ orbital in the UNEDF0, UNEDF1, and UNEDF2 is smaller. This may be caused by a larger effective mass of UNEDF EDFs. It should be noted that the larger effective mass makes the smaller energy spreading above the shell gap as well, while the UNEDF

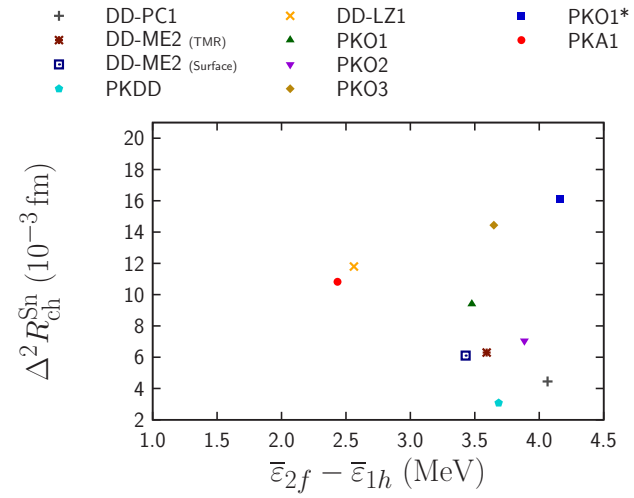

FIG. 13. Same as Fig. 12, but by using relativistic EDFs.

TABLE V. Same as Table II, but of Pb together with $\Delta R_{\rm ch}^{\rm Pb}(208)$ and $\Delta R_{\rm ch}^{\rm Pb}(210)$.

EDF	$\Delta R_{\rm ch}^{\rm Pb}(208)$	$\Delta R_{\rm ch}^{\rm Pb}(210)$	$\Delta^2 R_{\rm ch}^{\rm Pb}$
UNEDF0	+11.158	+9.561	−1.597
SkM*	+9.764	+9.491	−0.273
UNEDF1	+11.244	+11.364	+0.120
HFB9	+10.160	+10.945	+0.785
UNEDF2	+10.646	+11.670	+1.024
SLy4	+9.096	+11.210	+2.114
SLy5	+8.920	+11.507	+2.587
SGII	+9.396	+13.625	+4.229
SAMi-noT	+8.683	+16.457	+7.774
SAMi-T	+8.595	+16.829	+8.234
SAMi	+8.571	+18.176	+9.605
Expt.	+11.0	+19.6	+8.6

TABLE VI. Same as Table V, but by using relativistic EDFs.

EDF	$\Delta R_{\rm ch}^{\rm Pb}(208)$	$\Delta R_{\rm ch}^{\rm Pb}(210)$	$\Delta^2 R_{\rm ch}^{\rm Pb}$
PKA1	+8.709	+14.888	+6.179
DD-LZ1	+6.935	+15.462	+8.527
DD-ME2 (TMR)	+9.133	+17.962	+8.829
DD-ME2 (Surface)	+9.537	+18.567	+9.030
PKO2	+10.694	+19.800	+9.106
PKDD	+9.105	+19.879	+10.774
PKO3	+10.103	+21.265	+11.162
PKO1	+9.690	+21.183	+11.493
DD-PC1	+7.566	+20.118	+12.552
PKO1*	+10.553	+23.893	+13.340
Expt.	+11.0	+19.6	+8.6

series gives as wide energy spreading above the shell gap as the other Skyrme EDFs tested here. The spin-orbit strength, energy spreading, and the effective masses are related to each other [54]; hence, a detailed study of the effect of the effective mass is left for a future investigation. Another feature is the two parameters of the spin-orbit interaction in some of the Skyrme EDFs. Even though the strengths of isoscalar and isovector spin-orbit interactions, W_0 and W_0', are the same, the kink can appear as in the SGII case. Thus, the effect of W_0 and W_0' to the kink behavior is still puzzling. The tensor interactions also induce the spin-orbit mean field in the Skyrme EDF, SAMi-T, but its effect is tiny. The average single-particle energy of the $1h$ orbital is also correlated with the kink size.

It should be noted that these two orbitals, $2f_{7/2}$ and $1h_{9/2}$, are pseudospin doublet; thus if the pseudospin symmetry exactly holds, these two orbitals completely degenerate, which may make the occupation probability of $1h_{9/2}$ larger. It is known that the relativistic models have the pseudospin symmetry implicitly in the Dirac wave function. This may be another reason why the relativistic calculation describes the kink behavior better. However, some relativistic EDFs, such as the DD-LZ1, which is expected to give better description of the pseudospin symmetry, do not give such degeneration.

C. Pb isotopes

In this subsection, results for Pb isotopes are shown. The kink indicators for Pb isotopes are summarized in Tables V and VI. Results for Pb isotopes are basically similar to those for Sn isotopes, while there are some differences. For instance, HFB9 and UNEDF2 give small positive kinks, SGII and DD-PC1 give significantly larger kinks. Since properties of ^{208}Pb are frequently used for fitting criteria of EDFs, such differences may appear.

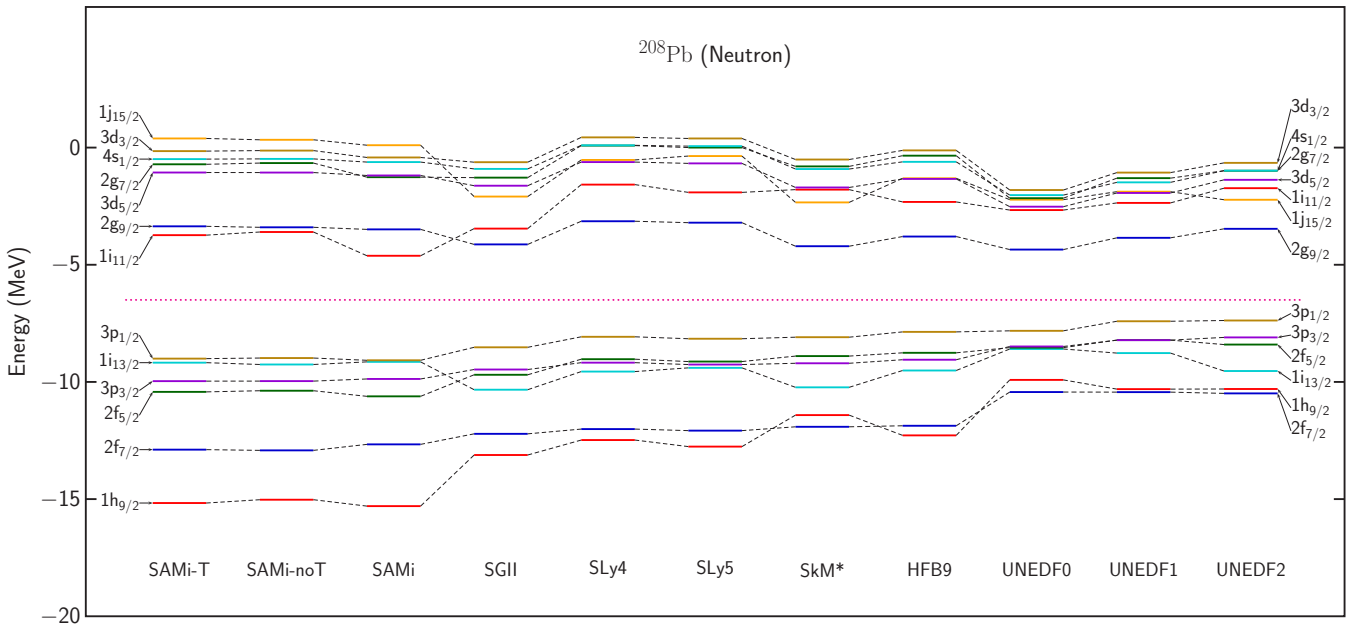

FIG. 14. Same as Fig. 5, but of ^{208}Pb.

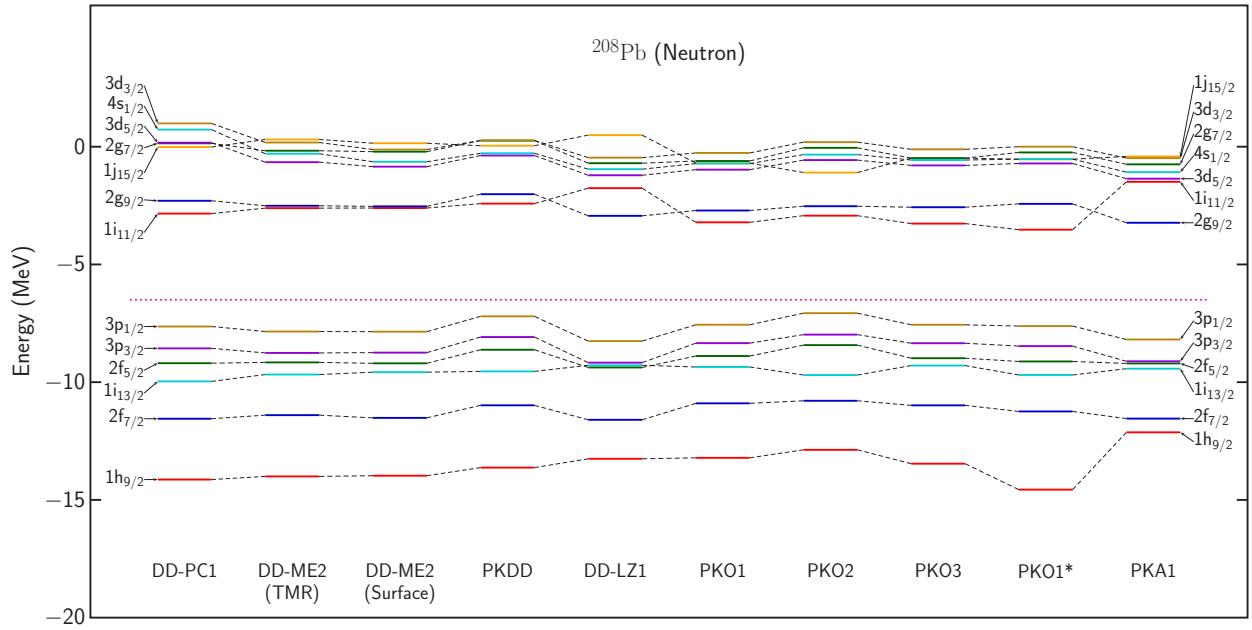

FIG. 15. Same as Fig. 14, but by using relativistic EDFs.

To understand these behaviors, the single-particle spectra of neutrons of ^{208}Pb are shown in Figs. 14 and 15. The magenta dotted line represents the $N = 126$ shell gap. All the calculations show that the $3p_{1/2}$ orbital is just below the $N = 126$ shell gap, while above the shell gap, either the $2g_{9/2}$ or $1i_{11/2}$ orbital appears: the SAMi-T, SAMi-noT, SAMi, DD-PC1, DD-ME2, PKDD, PKO1, PKO2, PKO3, and PKO1* EDFs give the $1i_{11/2}$ orbital lower than the $2g_{9/2}$ one, while the other calculations give the opposite. The exceptions are the SkM* and UNEDF2 EDFs. In these two EDFs, the $2g_{9/2}$ orbital appears just above the shell gap, the same as most Skyrme EDFs, but the $1j_{15/2}$ orbital appears instead of the $1i_{11/2}$ orbital above the $2g_{9/2}$ orbital. Referring to Tables V and VI, one can find that the EDFs, having the $1i_{11/2}$ orbital just above the shell gap, give a notable kink. Therefore, the order of the single-particle orbitals above the shell gap may play an important role as mentioned in Ref. [7]. To understand the mechanism more clearly, the occupation probabilities of the single-particle orbitals just above the shell gap of ^{210}Pb are plotted in Figs. 16 and 17. The correlation between the occupation probability of the $1i_{11/2}$ orbital and the slope above the $N = 126$ gap $[\Delta R_{\rm ch}^{\rm Pb}(210)]$ is plotted in Fig. 18. It is easily seen that, in general, the larger occupancy of the $1i_{11/2}$ orbital gives the steeper slope, and accordingly the larger kink. This mechanism is the same as discussed in Sn isotopes; the radial distribution of this single-particle orbital with a smaller n value can be extended and give a larger kink. We especially mention the DD-LZ1 and PKA1, which have relatively small kinks in Table VI. In the present case of Pb, this small kink is attributable to the occupation probabilities shown in Fig. 18. Namely, the dominant component is of $2g_{9/2}$ with DD-LZ1 and PKA1, whereas the other relativistic EDFs conclude the dominance of $1i_{11/2}$. Then, the dominant $1i_{11/2}$ ($2g_{9/2}$) component leads to a large (small) change of radii for the corresponding kink behavior. However, as we mentioned in the previous Sn case, this explanation was less persuading for the Sn isotopes, where the DD-LZ1 and PKA1 conclude large kinks, even though their occupation probabilities of $1h_{9/2}$ for extended radii are minor, as shown in Fig. 8.

The SGII EDF gives the notable kink, while the $2g_{9/2}$ orbital appears just above the $N = 126$ shell gap. Nevertheless, this can be understood as follows: the energy difference between the $2g_{9/2}$ orbital and the $1i_{11/2}$ one is small for the SGII case compared with the other calculations. Accordingly, as seen in Fig. 16, the occupation probability of $1i_{11/2}$ is substantially large, even though that of $2g_{9/2}$ is larger than $1i_{11/2}$. Hence, the effect of the $1i_{11/2}$ orbital is appreciable. Then, one puzzle appears. Even though the strengths of isoscalar and isovector spin-orbit interactions, W_0 and W_0', are the same in the SGII EDF, the kink can appear in almost the same size with the SAMi EDF, in which $W_0 \neq W_0'$. This is in con-

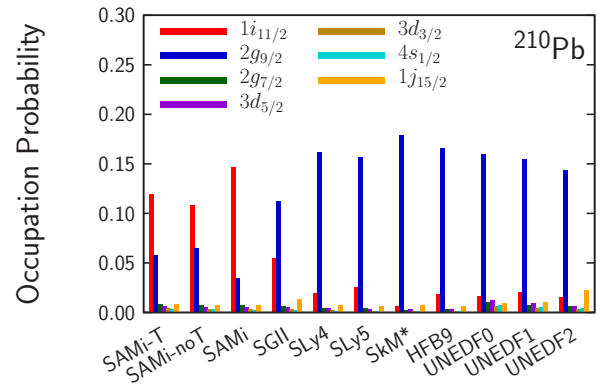

FIG. 16. Occupation probability of orbitals above the $N = 126$ shell gap for ^{210}Pb calculated by using nonrelativistic EDFs.

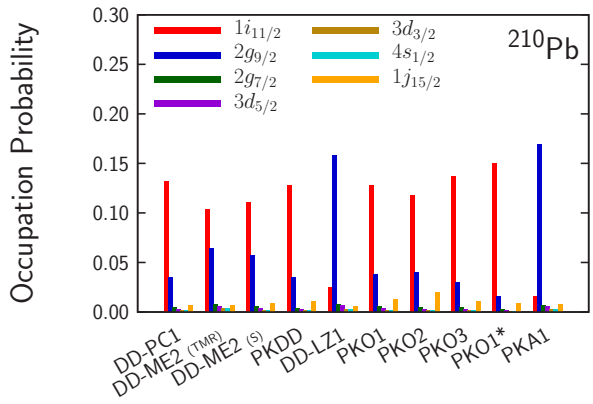

FIG. 17. Same as Fig. 16, but by using relativistic EDFs.

trast to the claim in Refs. [5,46]. Thus, we cannot find any strong relation between the isoscalar and isovector spin-orbit strengths and the kink behavior. Lastly, we should notice that the Skyrme tensor interaction also introduces the spin-orbit mean field of SAMi-T, but its effect is tiny, as in the Sn case.

Figures 19 and 20 show the correlation between the averaged single-particle energies $\overline{\varepsilon}$ of the $1i$ and $2g$ orbitals in ^{210}Pb and the kink size $\Delta^2 R_{\rm ch}$. There is a weak correlation between $\overline{\varepsilon}$ of the $1i$ orbital and the kink size. This can be understood that, as $\overline{\varepsilon}$ of the $1i$ orbital is small, the $1i_{11/2}$ orbital becomes lower and accordingly the occupation probability of the $1i_{11/2}$ orbital becomes larger. The occupation probability of the $1i_{11/2}$ orbitals is correlated to the kink size as discussed above. In contrast to the case of ^{134}Sn, there is also a weak correlation between $\overline{\varepsilon}$ of the $2g$ orbital and the kink size; while the correlation is opposite to that for the $1i$ orbital. In Figs. 21 and 22, the correlation between the difference between two average energies, $\overline{\varepsilon}_{2g} - \overline{\varepsilon}_{1i}$, and the kink size is shown. We found that there is an obvious correlation between $\overline{\varepsilon}_{2g} - \overline{\varepsilon}_{1i}$ and $\Delta^2 R_{\rm ch}^{\rm Pb}$ in both the nonrelativistic and relativistic calculations. This clearly indicates that the kink size $\Delta^2 R_{\rm ch}^{\rm Pb}$ also depends on properties of the central nuclear potential as well.

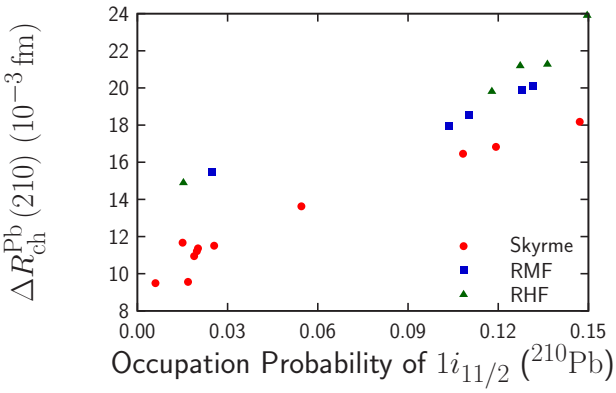

FIG. 18. Correlation between occupation probability of $1i_{11/2}$ orbital of ^{210}Pb and kink size at $N = 126$.

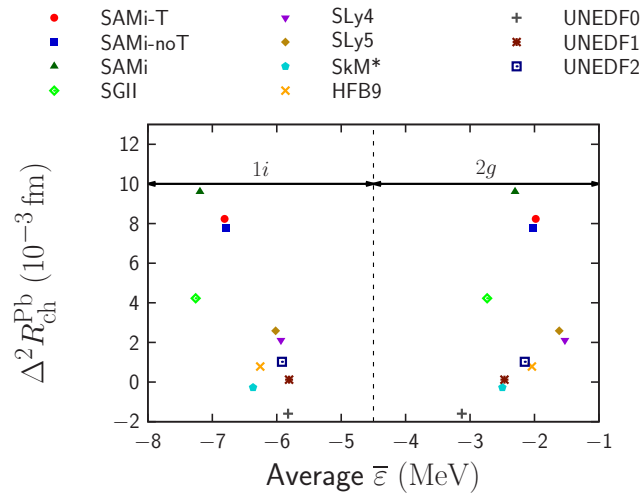

FIG. 19. Correlation between the averaged single-particle energies of $1i$ and $2g$ orbitals of ^{210}Pb and the kink size calculated by using nonrelativistic EDFs.

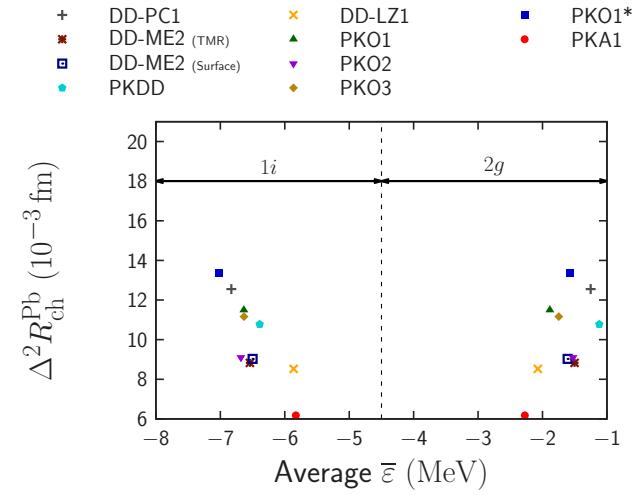

FIG. 20. Same as Fig. 19, but by using relativistic EDFs.

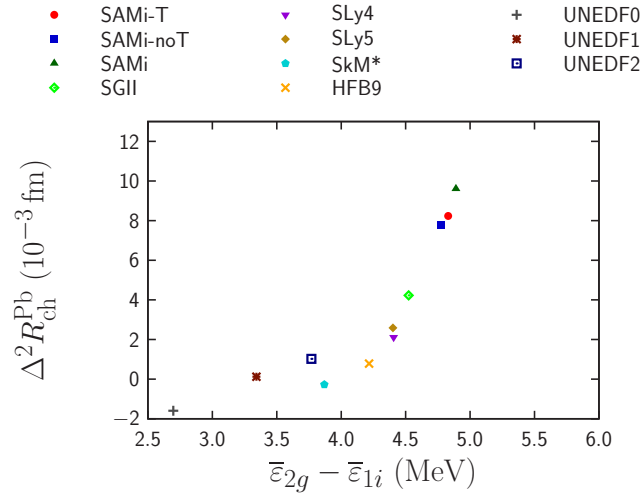

FIG. 21. Correlations between the difference between the averaged single-particle energies of $1i$ and $2g$ orbitals of ^{210}Pb and the kink size calculated by using nonrelativistic EDFs.

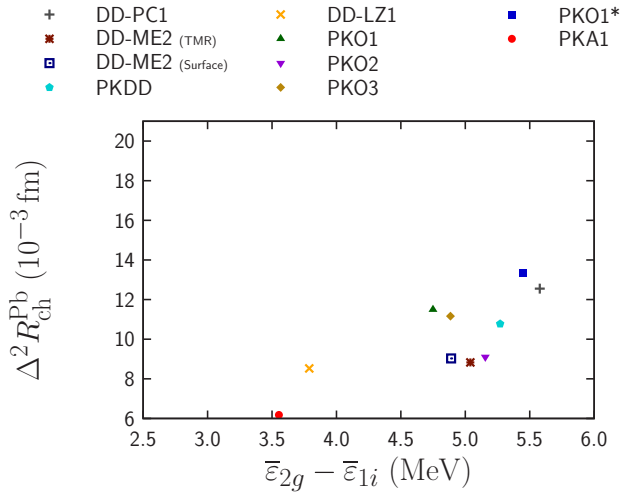

FIG. 22. Same as Fig. 21, but by using relativistic EDFs.

D. Parameters of nuclear equation of state

Next, we will discuss whether parameters of the equation of state (EoS) affect the kink behavior. The SAMi EDF has three families: SAMi-J, SAMi-m, and SAMi-K families. In these families, the fitting protocol of the EDF parameters is basically the same as the original SAMi EDF, besides one of the EoS parameters is fixed to be a selected value: each member of the SAMi-J family assumes a different symmetry energy coefficient J at the saturation density, the SAMi-m member assumes the different effective mass m^*, and the SAMi-K member assumes the different incompressibility K_∞. Figures 23–25, respectively, show the slope $\Delta R_{\rm ch}^{\rm Sn}$ as functions of the mass number A for the SAMi-J, SAMi-m, and SAMi-K families. If the value of $\Delta R_{\rm ch}$ increases sharply at $A = A_{\rm magic}$, the large kink appears at the magic number $A_{\rm magic}$. The results of the SAMi-K family show an almost complete overlap with each other below the $N = 82$ gap, while they show tiny differences above the gap although there is no clear tendency of K_∞. Therefore, it can be concluded that the

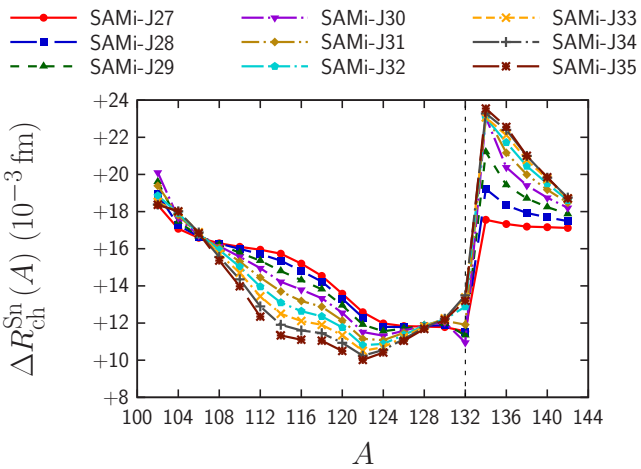

FIG. 23. Relative change of charge radii $\Delta R_{\rm ch}$ of Sn isotopes as a function of A calculated by using the SAMi-J family.

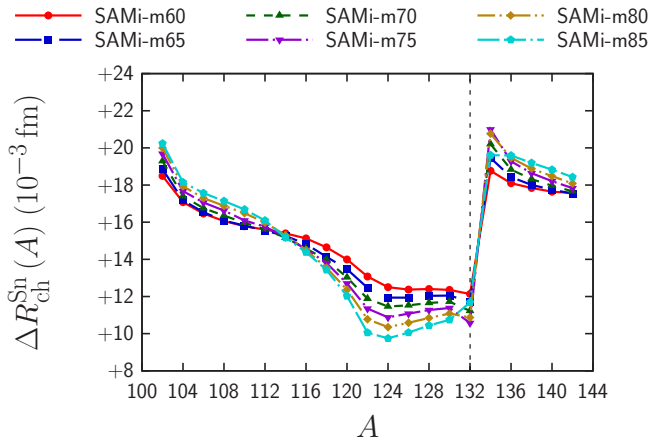

FIG. 24. Same as Fig. 23, but by using the SAMi-m family.

incompressibility K_∞ scarcely has any visible impact on the value $R_{\rm ch}$. Different SAMi-m EDF gives similar $\Delta R_{\rm ch}$ above the $N = 82$ gap but slightly different tendency in the region $66 \leqslant N \leqslant 82$. This may be because the effective mass changes the level distance between single-particle states, which leads to the different occupancy. Accordingly, the smaller effective mass gives smaller kink, but its effect is minor. The size of kink simultaneously depends on the level spacing, which is not attributable only to the effective mass but also to other parameters [54].

Different SAMi-J EDF gives slightly different behavior of $\Delta R_{\rm ch}$ above the $N = 82$ gap. For simplicity, let us assume that all the SAMi-J EDFs give the same $R_{\rm ch}$ at $N = 82$. Then, naturally, a larger symmetry energy gives a larger neutron radius of ^{132}Sn. Adding two neutrons to ^{132}Sn, these two neutrons change the proton radius due to the proton-neutron interaction, which is strongly related to the symmetry energy. The larger neutron radius leads to the larger proton radius of ^{134}Sn. In addition, the proton-neutron interaction between the last two neutrons and the protons is important. As a net effect, the larger J gives the larger $R_{\rm ch}$ at $N > 82$, as mentioned in Ref. [9] for mercury isotopes.

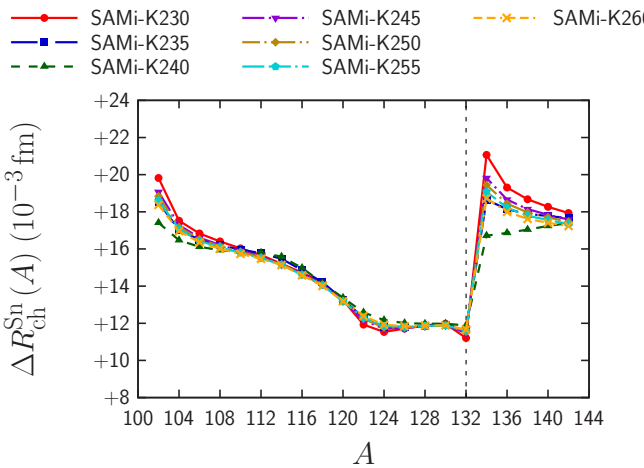

FIG. 25. Same as Fig. 23, but by using the SAMi-K family.

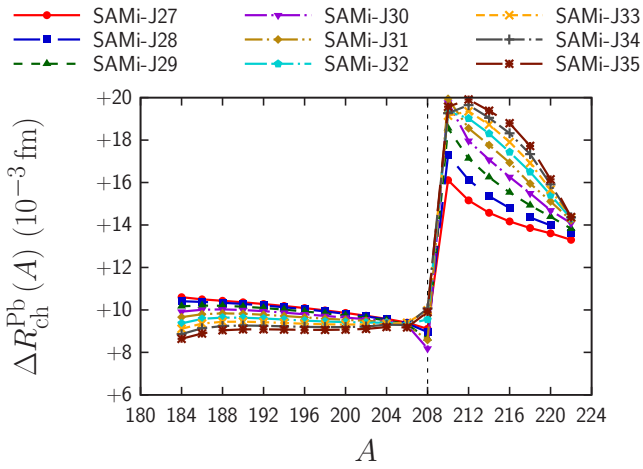

FIG. 26. Same as Fig. 23, but for Pb isotopes.

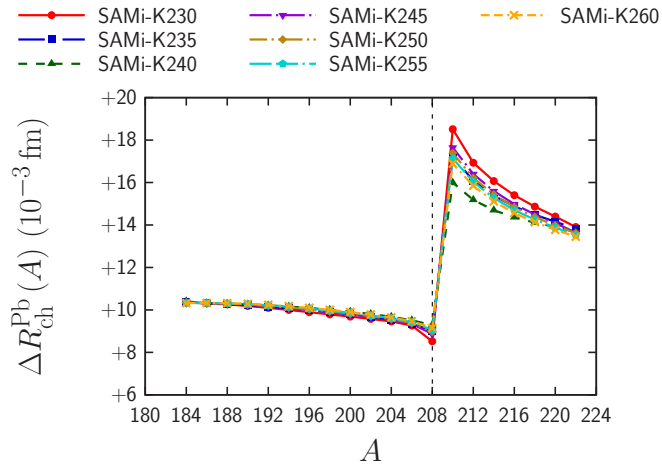

FIG. 28. Same as Fig. 25, but for Pb isotopes.

The similar results can be found in Pb isotopes, while all the parameter sets give the similar results below the $N = 126$ magic number, as shown in Figs. 26–28.

E. Pairing interaction and its strength

We will discuss now whether the pairing strength affects the kink behavior. Figures 29 and 30, respectively, show the slope $\Delta R_{\rm ch}^{\rm Sn}$ and $\Delta R_{\rm ch}^{\rm Pb}$ as functions of the mass number A for different pairing strengths of the volume-type pairing with the SAMi EDF and Table VII shows the kink indicators for both Sn and Pb isotopes. Here, $V_0 = 213.7\,\text{MeV fm}^3$ is the adopted strength, which reproduces the neutron pairing gap of ^{120}Sn as 1.4 MeV. Note that the calculation without the pairing ($V_0 = 0\,\text{MeV fm}^3$) does not reach convergence; thus, the results are not shown here. Although the behaviors below or above the shell gap are different for different pairing strengths, results calculated with weaker pairing strengths give similar behavior around the magic numbers. The kink indicator $\Delta^2 R_{\rm ch}$ is larger if the pairing strength is stronger for Sn isotopes, while the opposite behavior is shown for Pb isotopes. Note that results with $V_0 = 250$ and $300\,\text{MeV fm}^3$ give different

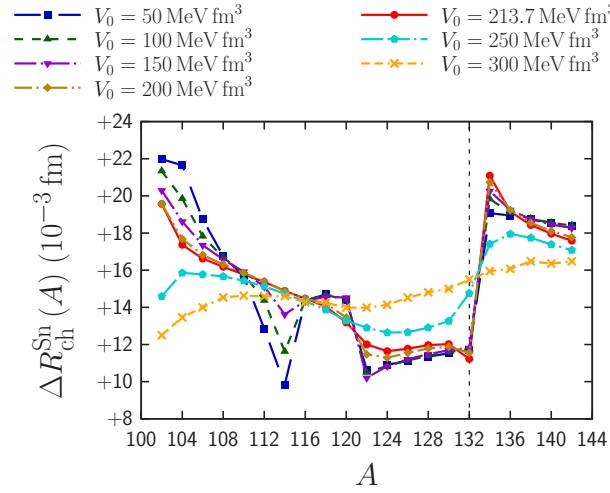

FIG. 29. Relative change of charge radii $\Delta R_{\rm ch}$ of Sn isotopes as a function of A for different pairing strengths of the volume-type pairing with the SAMi EDF.

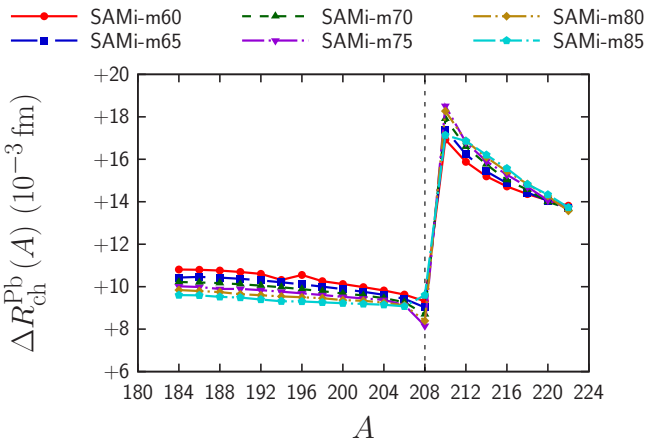

FIG. 27. Same as Fig. 24, but for Pb isotopes.

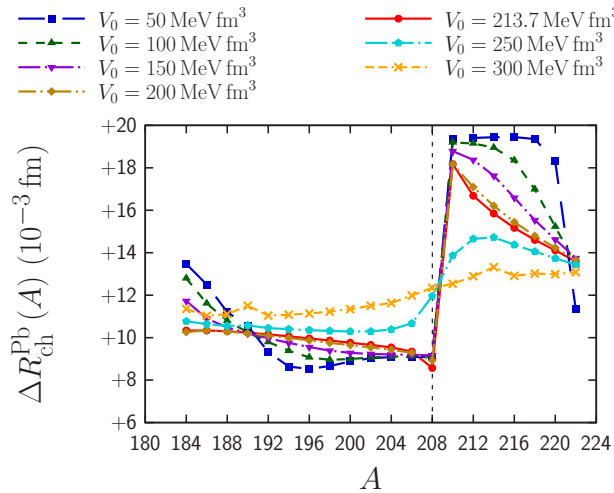

FIG. 30. Same as Fig. 29, but for Pb isotopes.

TABLE VII. Kink indicator $\Delta^2 R_{\rm ch}^{\rm Sn}$ and $\Delta^2 R_{\rm ch}^{\rm Pb}$ for Sn and Pb calculated by the nonrelativistic SAMi EDF with various pairing strength of the volume-type pairing are also listed. All values are given in units of 10^{-3} fm.

Strength V_0	$\Delta^2 R_{\rm ch}^{\rm Sn}$	$\Delta^2 R_{\rm ch}^{\rm Pb}$
50	+7.381	+10.257
100	+8.066	+10.071
150	+8.445	+9.626
200	+9.185	+9.245
213.7	+9.863	+9.605
250	+2.646	+1.914
300	+0.441	+0.183

behavior. This is because they give the finite pairing gap even for ^{132}Sn and ^{208}Pb, i.e., ^{132}Sn and ^{208}Pb are no longer magic nuclei. Therefore, it is concluded that the pairing strength does not affect the kink behavior strongly, as long as the magicity remains unchanged.

Figures 31 and 32, respectively, show the slope $\Delta R_{\rm ch}^{\rm Sn}$ and $\Delta R_{\rm ch}^{\rm Pb}$ as a function of the mass number A for different types of pairing interaction with the SAMi EDF. Table VIII shows the kink indicates for both Sn and Pb isotopes. Here, the pairing interaction used is written as

$$V_{\rm pair}(\boldsymbol{r}) = -V_0\left(1-\alpha\frac{\rho(\boldsymbol{r})}{\rho_0}\right)\delta(\boldsymbol{r}), \tag{6}$$

where $\rho_0 = 0.16\,{\rm fm}^{-3}$ is the saturation density and $\alpha = 0$, $1/2$, and 1, respectively, correspond to the volume-type, mixed-type, and surface-type pairings. The strengths V_0 are, respectively, 213.7, 322.4, and 558.0 MeV fm^3 for volume-type, mixed-type, and surface-type pairings, which are determined to reproduce the neutron pairing gap of ^{120}Sn as 1.4 MeV. It is seen in the figures that, as long as these volume-type, mixed-type, and surface-type pairings are used, no significant difference can be found, while the mixed pairing shows the strongest kink indicator. Note that the pairing gaps of ^{132}Sn obtained by the mixed-type and surface-type pairings are, respectively, 0.50 and 1.47 MeV and that of ^{208}Pb

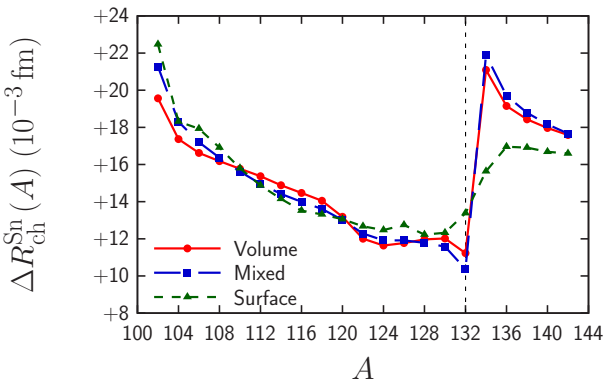

FIG. 31. Relative change of charge radii $\Delta R_{\rm ch}$ of Sn isotopes as a function of A for different types of pairing interactions with the SAMi EDF.

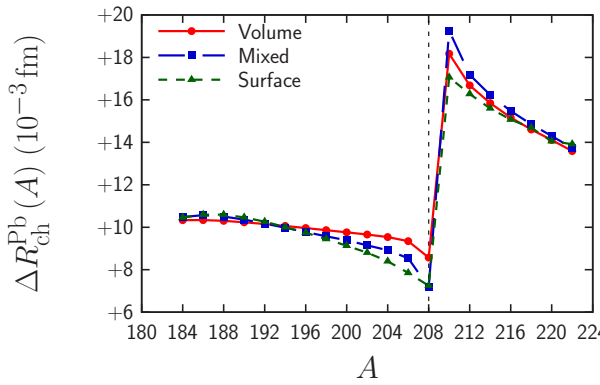

FIG. 32. Same as Fig. 31, but for Pb isotopes.

obtained by the surface-type pairing is 0.55 MeV. These finite gaps mean that the magicities of these nuclei are effectively broken by the pairing correlations.

F. Ca isotopes

The mass number A dependence of $R_{\rm ch}^{\rm Ca}(A) - R_{\rm ch}^{\rm Ca}(48)$ for Ca isotopes calculated by nonrelativistic (SHF) and relativistic (RMF and RHF) EDFs are shown in Figs. 33 and 34, respectively. For comparison, experimental data [55,56] are also plotted. The kink sizes for Ca isotopes are summarized in Tables IX and X.

We can see that the kink evolution of Ca isotopes, especially, around the $N = 28$ kink, is quite different from those of Sn and Pb isotopes. Compared with the calculated results, the systematic behavior of experimental $R_{\rm ch}$ values, even $N < 28$, is not well described. Indeed, it is suggested in several works [7,57,58] that beyond-mean-field effects are important in Ca isotopes. This is an open and intriguing problem for the microscopic model beyond mean field.

IV. CONCLUSION

In this paper, the sudden change of the mass-number dependence of the charge radius at the neutron shell gap, the so-called kink behavior, is discussed for Sn and Pb isotopes by using the nonrelativistic Skyrme, relativistic mean field (RMF), and the relativistic Hartree-Fock (RHF) calculations. In general, the RHF calculations give the larger kink with positive kink indicators and the Skyrme calculations give the smaller positive values. One exception among the Skyrme EDFs is the SAMi series which gives exceptionally larger kink. Abnormal behavior of the kink is induced by some Skyrme EDFs, for instance, the UNEDF series, which give

TABLE VIII. Same as Table VII but for the different pairing interaction.

Type of pairing interaction	$\Delta^2 R_{\rm ch}^{\rm Sn}$	$\Delta^2 R_{\rm ch}^{\rm Pb}$
Volume	+9.863	+9.605
Mixed	+11.526	+12.085
Surface	+2.251	+9.812

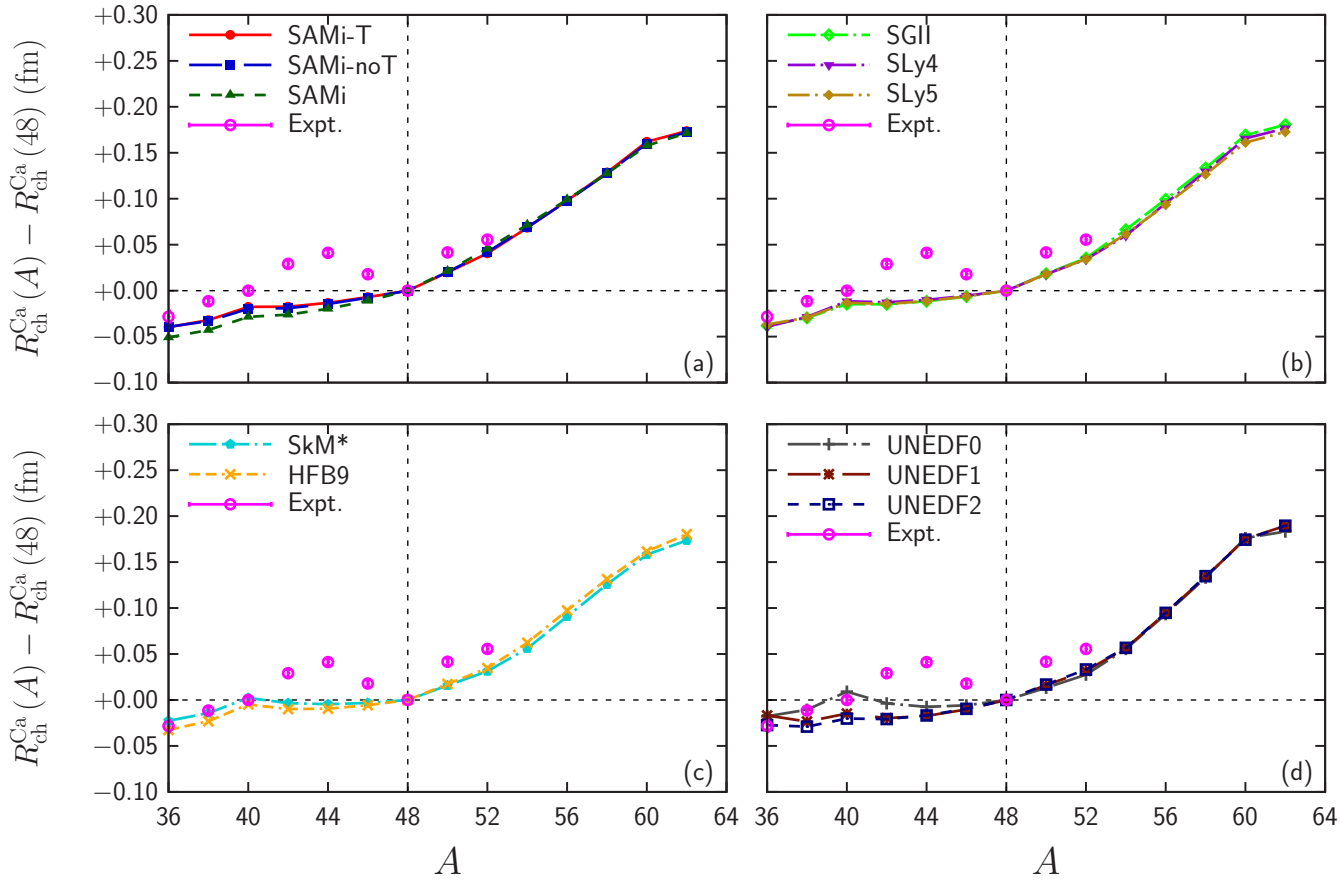

FIG. 33. Same as Fig. 1, but for Ca isotopes. Experimental data except ^{40}Ca are taken from Refs. [55,56], instead of Ref. [3].

the opposite behavior, a negative value for the kink indicator. In order to reproduce the kink behavior for the Sn isotopes, the occupation probability of the $1h_{9/2}$ orbital should be large enough. On the other hand, if the occupation probability of the $3p_{3/2}$ orbital is large, the antikink may appear. In the case of Pb isotopes, a larger occupation probability of the $1i_{11/2}$ orbital gives a larger kink indicator at the $N = 126$ shell gap. To make such occupancy, the spin-orbit mean-field must not be too strong. Note that the averaged value of the single-particle energy for the spin-orbit doublet also affects the occupation probability.

Analyzing the RHF calculation, the tensor interaction, which contributes to the spin-orbit mean-field potential, is concluded as an essential ingredient to produce such proper occupations of the single-particle states and to reproduce well the kink behavior. Compared with the tensor effect of RHF, the effect of the Skyrme tensor interaction in SAMi-T EDF is found to be tiny. The different strengths between

TABLE IX. Same as Table II, but of Ca together with $\Delta R^{\rm Ca}_{\rm ch}(48)$ and $\Delta R^{\rm Ca}_{\rm ch}(50)$.

EDF	$\Delta R^{\rm Ca}_{\rm ch}(48)$	$\Delta R^{\rm Ca}_{\rm ch}(50)$	$\Delta^2 R^{\rm Ca}_{\rm ch}$
UNEDF1	+10.272	+15.999	+5.727
UNEDF2	+9.611	+16.829	+7.218
UNEDF0	+5.814	+13.268	+7.454
SAMi	+11.096	+21.330	+10.234
HFB9	+5.729	+17.407	+11.678
SLy5	+6.153	+18.080	+11.927
SGII	+6.334	+18.378	+12.044
SLy4	+5.421	+17.856	+12.435
SAMi-noT	+7.702	+20.374	+12.672
SKMs	+3.182	+15.861	+12.679
SAMi-T	+6.976	+19.841	+12.865
Expt.	−17.8	+41.5	+59.3

TABLE X. Same as Table IX, but by using relativistic EDFs.

EDF	$\Delta R^{\rm Ca}_{\rm ch}(48)$	$\Delta R^{\rm Ca}_{\rm ch}(50)$	$\Delta^2 R^{\rm Ca}_{\rm ch}$
DD-PC1	+3.671	+16.293	+12.622
PKDD	+1.674	+19.694	+18.020
PKO2	+2.670	+24.965	+22.295
DD-ME2 (Surface)	−0.019	+24.576	+24.595
PKO1*	−2.174	+23.201	+25.375
PKO1	−0.956	+25.284	+26.240
DD-ME2 (TMR)	−1.631	+25.863	+27.494
PKO3	−0.550	+27.110	+27.660
DD-LZ1	−10.279	+31.533	+41.812
PKA1	−15.149	+29.323	+44.472
Expt.	−17.8	+41.5	+59.3

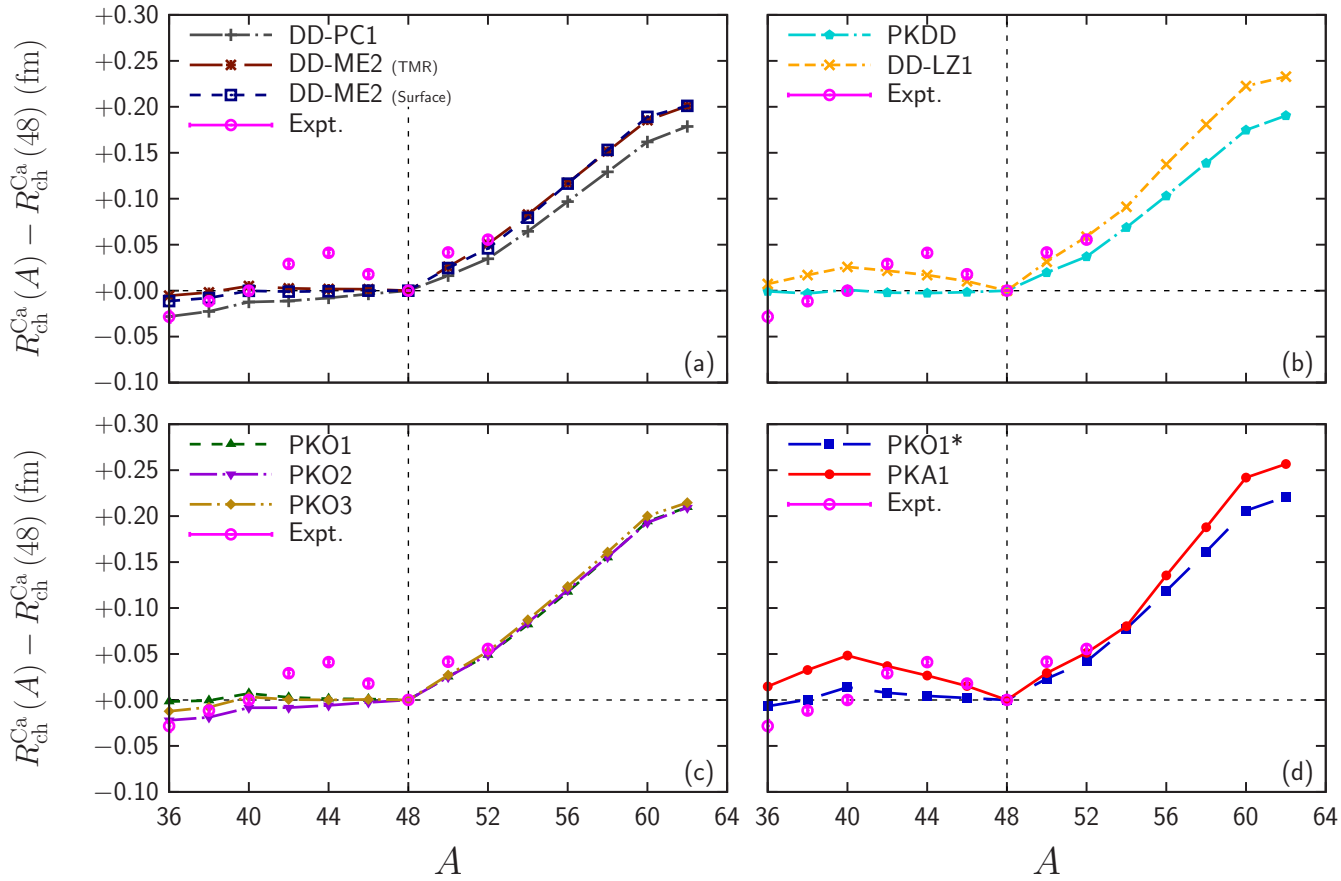

FIG. 34. Same as Fig. 2, but for Ca isotopes. Experimental data except ^{40}Ca are taken from Refs. [55,56], instead of Ref. [3].

the isoscalar and isovector spin-orbit interactions in the Skyrme EDF, $W_0 \neq W_0'$, may not be an absolutely necessary condition to reproduce the kink behavior, since the kink can be produced even by some Skyrme EDFs with $W_0 = W_0'$ spin-orbit interactions. Hence, the proper determination of the strength of the isoscalar and isovector spin-orbit interactions is demanded. Considering the reference data for this interest, experimentally these spin-orbit interactions manifest themselves in the spin-orbit splittings of odd-mass nuclei. However, these levels are affected by the particle-vibration coupling [59], which is not considered in this paper. It should be noted that the isovector-scalar δ meson can also introduce the spin-orbit interaction with the isospin dependence [7,60–62]. As shown in Ref. [7], the δ meson in the RMF calculation is an alternative way to reproduce the kink.

We also investigated whether parameters of nuclear equation of state affect such kink behavior. It is found that the symmetry energy affects appreciably to change the magnitude of the kink indicator in a similar way to induce the neutron-skin thickness. The effective masses affect the kink behavior slightly; smaller effective mass gives smaller kink. In contrast, the nuclear incompressibility scarcely affects the kink behavior.

Mass number dependence of the charge radii of Ca isotopes is rather different from those Sn or Pb isotopes, which implies the importance of beyond-mean-field effects.

The form of the pairing interaction is still under debate. For instance, the derivative dependence such as the Fayans-type [63,64], isoscalar pairing [65–71], and spin-triplet pairing [72–74] have been discussed recently. The pairing strength for the deformed nuclei might be different from that for the spherical nuclei [71,75,76]. Effects of them to the kink behavior are left for future perspectives. The beyond-mean-field effect can also affect the kink behavior [7,9,10], which is out of the scope of this paper and remains for future perspectives, since we focused only on the mean-field level in this paper.

ACKNOWLEDGMENTS

The authors acknowledge for the fruitful discussion with Andrei Andreyev, Nobuo Hinohara, Tsunenori Inakura, Hitoshi Nakada, and Qiang Zhao. The authors also thank Xavier Roca-Maza for allowing us to use the SAMi-J, SAMi-K, and SAMi-m families. T.N. acknowledges the RIKEN Special Postdoctoral Researcher Program, the Science and Technology Hub Collaborative Research Program from RIKEN Cluster for Science, Technology and Innovation Hub (RCSTI), the JSPS Grant-in-Aid for Research Activity Start-up under Grant No. 22K20372, the JSPS Grant-in-Aid for Transformative Research Areas (A) under Grant No. 23H04526, the JSPS Grant-in-Aid for Scientific Research (B) under Grant No. 23H01845, and the JSPS

Grant-in-Aid for Scientific Research (C) under Grant No. 23K03426. T.O. acknowledges the support of the Yukawa Research Fellow Programme by Yukawa Memorial Foundation. H.S. acknowledges the JSPS Grant-in-Aid for Scientific Research (C) under Grant No. 19K03858. Z.W. acknowledges the support of the Natural Science Foundation of China under Grants No. 11905088 and No. 12275111. The numerical calculations were partly performed on cluster computers at the RIKEN iTHEMS program.

APPENDIX: SPIN-ORBIT CONTRIBUTION OF CHARGE RADII

The fourth and fifth terms of Eq. (2) are called the spin-orbit contributions, originating from the nucleon magnetic moments. These terms have not been considered in most works [18], while it was also discussed that these terms are not negligible if one discusses the tiny contribution or compare with the experimental data precisely [40,77,78]. In this Appendix, we will discuss the effect of the spin-orbit contribution to nuclear charge radii and their kink behavior for Sn and Pb isotopes.

The spin-orbit contribution of charge radii is [40,77]

$$\langle r^2\rangle_{\mathrm{SO}\tau} \simeq \frac{\kappa_\tau}{M_\tau^2 N_\tau} \sum_{a\in\mathrm{occ}} \mathcal{N}_{a\tau}\langle \boldsymbol{l}\cdot\boldsymbol{\sigma}\rangle, \tag{A1}$$

where $N_\tau = Z$ for $\tau = p$, $N_\tau = N$ for $\tau = n$, κ_τ and M_τ are, respectively, the magnetic moment and the mass of nucleons τ, and $\mathcal{N}_{a\tau}$ is the occupation number of the orbital a. It is obvious that the s orbitals do not contribute to $\langle r^2\rangle_{\mathrm{SO}\tau}$; if the spin-orbit doublets are completely occupied, contribution of these two orbitals cancel each other out. Therefore, only the spin-orbit doublets partially occupied contributes to $\langle r^2\rangle_{\mathrm{SO}\tau}$.

The proton spin-orbit contribution to the charge radius, $\langle r^2\rangle_{\mathrm{SO}p}$, is rather simple. Only the $1g_{9/2}$ orbital ($\langle \boldsymbol{l}\cdot\boldsymbol{\sigma}\rangle = +4$, $\mathcal{N}_a = 10$) and only the $1h_{11/2}$ orbital ($\langle \boldsymbol{l}\cdot\boldsymbol{\sigma}\rangle = +5$, $\mathcal{N}_a = 12$), respectively, contribute to $\langle r^2\rangle_{\mathrm{SO}p}$ in Sn and Pb isotopes; hence, the contribution can be, respectively, estimated as $\langle r^2\rangle_{\mathrm{SO}p} = 0.0634\,\mathrm{fm}^2$ and $0.0580\,\mathrm{fm}^2$. These contributions are common for each isotopic chain, and thus the proton spin-orbit contribution just shifts the graphs of Figs. 1, 2, 3, and 4 upwards, and the kink behaviors are not changed.

In contrast, the spin-orbit contributions of the neutrons $\langle r^2\rangle_{\mathrm{SO}n}$ affect the kink behavior. Note that the magnetic moment of neutrons κ_n is negative. First, let us focus on Sn isotopes. Below the $N = 82$ shell gap, the highest orbital is the $1h_{11/2}$ orbital ($\langle \boldsymbol{l}\cdot\boldsymbol{\sigma}\rangle = +5$), which gives the negative $\langle r^2\rangle_{\mathrm{SO}n}$ of $N < 82$ isotopes, and thus, the slope below $N = 82$ becomes mild if the spin-orbit contribution is considered. In contrast, above the $N = 82$ shell gap, either the $1h_{9/2}$ orbital ($\langle \boldsymbol{l}\cdot\boldsymbol{\sigma}\rangle = -6$), the $2f_{7/2}$ orbital ($\langle \boldsymbol{l}\cdot\boldsymbol{\sigma}\rangle = +3$), or $3p_{3/2}$ orbital ($\langle \boldsymbol{l}\cdot\boldsymbol{\sigma}\rangle = +1$) are mainly occupied. If the $1h_{9/2}$ orbital is mainly occupied in $N > 82$ isotopes, the spin-orbit contribution leads to the slope above $N = 82$ steep, and thus the kink becomes strong. On the contrary, if the $2f_{7/2}$ or $3p_{3/2}$ orbital is mainly occupied in $N > 82$ isotopes, the spin-orbit contribution leads to the slope above $N = 82$ mild, but the kink becomes slightly strong.

In the case of Pb isotopes, below the $N = 126$ shell gap, the highest orbital is the $3p_{1/2}$ orbital ($\langle \boldsymbol{l}\cdot\boldsymbol{\sigma}\rangle = -2$), which gives the positive $\langle r^2\rangle_{\mathrm{SO}n}$ of $N < 126$ isotopes, and thus, the slope below $N = 126$ becomes steep if the spin-orbit contribution is considered. In contrast, above the $N = 126$ shell gap, either the $1i_{11/2}$ orbital ($\langle \boldsymbol{l}\cdot\boldsymbol{\sigma}\rangle = -7$), the $2g_{9/2}$ orbital ($\langle \boldsymbol{l}\cdot\boldsymbol{\sigma}\rangle = +4$), and $1j_{15/2}$ orbital ($\langle \boldsymbol{l}\cdot\boldsymbol{\sigma}\rangle = +7$) are mainly occupied. If the $1i_{11/2}$ orbital is mainly occupied in $N > 126$ isotopes, the spin-orbit contribution leads to the slope above $N = 126$ steep, and thus the kink becomes strong. On the contrary, if the $2g_{9/2}$ or $1j_{15/2}$ orbital is mainly occupied in $N > 126$ isotopes, which leads to the slope above $N = 126$ mild, the kink becomes weak.

[1] H. De Vries, C. W. De Jager, and C. De Vries, Nuclear charge-density-distribution parameters from elastic electron scattering, At. Data Nucl. Data Tables **36**, 495 (1987).
[2] T. Suda and H. Simon, Prospects for electron scattering on unstable, exotic nuclei, Prog. Part. Nucl. Phys. **96**, 1 (2017).
[3] I. Angeli and K. P. Marinova, Table of experimental nuclear ground state charge radii: An update, At. Data Nucl. Data Tables **99**, 69 (2013).
[4] P. Campbell, I. D. Moore, and M. R. Pearson, Laser spectroscopy for nuclear structure physics, Prog. Part. Nucl. Phys. **86**, 127 (2016).
[5] P.-G. Reinhard and H. Flocard, Nuclear effective forces and isotope shifts, Nucl. Phys. A **584**, 467 (1995).
[6] H. Nakada, Irregularities in nuclear radii at magic numbers, Phys. Rev. C **100**, 044310 (2019).
[7] U. C. Perera, A. V. Afanasjev, and P. Ring, Charge radii in covariant density functional theory: A global view, Phys. Rev. C **104**, 064313 (2021).
[8] B. A. Marsh, T. Day Goodacre, S. Sels, Y. Tsunoda, B. Andel, A. N. Andreyev, N. A. Althubiti, D. Atanasov, A. E. Barzakh, J. Billowes, K. Blaum, T. E. Cocolios, J. G. Cubiss, J. Dobaczewski, G. J. Farooq-Smith, D. V. Fedorov, V. N. Fedosseev, K. T. Flanagan, L. P. Gaffney, L. Ghys *et al.*, Characterization of the shape-staggering effect in mercury nuclei, Nat. Phys. **14**, 1163 (2018).
[9] T. Day Goodacre, A. V. Afanasjev, A. E. Barzakh, L. Nies, B. A. Marsh, S. Sels, U. C. Perera, P. Ring, F. Wienholtz, A. N. Andreyev, P. Van Duppen, N. A. Althubiti, B. Andel, D. Atanasov, R. S. Augusto, J. Billowes, K. Blaum, T. E. Cocolios, J. G. Cubiss, G. J. Farooq-Smith *et al.*, Charge radii, moments, and masses of mercury isotopes across the $N = 126$ shell closure, Phys. Rev. C **104**, 054322 (2021).
[10] T. DayGoodacre, A. V. Afanasjev, A. E. Barzakh, B. A. Marsh, S. Sels, P. Ring, H. Nakada, A. N. Andreyev, P. VanDuppen, N. A. Althubiti, B. Andel, D. Atanasov, J. Billowes, K. Blaum, T. E. Cocolios, J. G. Cubiss, G. J. Farooq-Smith, D. V. Fedorov, V. N. Fedosseev, K. T. Flanagan, L. P. Gaffney, L. Ghys, M. Huyse, S. Kreim, D. Lunney, K. M. Lynch, V. Manea, Y. MartinezPalenzuela, P. L. Molkanov, M. Rosenbusch, R. E. Rossel, S. Rothe, L. Schweikhard, M. D. Seliverstov,

P. Spagnoletti, C. VanBeveren, M. Veinhard, E. Verstraelen, A. Welker, K. Wendt, F. Wienholtz, R. N. Wolf, A. Zadvornaya, and K. Zuber, Laser Spectroscopy of Neutron-Rich ^{207,208}Hg Isotopes: Illuminating the Kink and Odd-Even Staggering in Charge Radii across the $N = 126$ Shell Closure, Phys. Rev. Lett. **126**, 032502 (2021).

[11] D. Vautherin and D. M. Brink, Hartree-Fock calculations with Skyrme's interaction. I. Spherical nuclei, Phys. Rev. C **5**, 626 (1972).

[12] L. D. Miller and A. E. S. Green, Relativistic self-consistent meson field theory of spherical nuclei, Phys. Rev. C **5**, 241 (1972).

[13] J. D. Walecka, A theory of highly condensed matter, Ann. Phys. **83**, 491 (1974).

[14] W.-H. Long, N. Van Giai, and J. Meng, Density-dependent relativistic Hartree-Fock approach, Phys. Lett. B **640**, 150 (2006).

[15] W. H. Long, P. Ring, N. Van Giai, and J. Meng, Relativistic Hartree-Fock-Bogoliubov theory with density dependent meson-nucleon couplings, Phys. Rev. C **81**, 024308 (2010).

[16] X. Roca-Maza, G. Colò, and H. Sagawa, New Skyrme interaction with improved spin-isospin properties, Phys. Rev. C **86**, 031306(R) (2012).

[17] N. Van Giai and H. Sagawa, Spin-isospin and pairing properties of modified Skyrme interactions, Phys. Lett. B **106**, 379 (1981).

[18] E. Chabanat, P. Bonche, P. Haensel, J. Meyer, and R. Schaeffer, A Skyrme parametrization from subnuclear to neutron star densities Part II. Nuclei far from stabilities, Nucl. Phys. A **635**, 231 (1998).

[19] J. Bartel, P. Quentin, M. Brack, C. Guet, and H.-B. Håkansson, Towards a better parametrisation of Skyrme-like effective forces: A critical study of the SkM force, Nucl. Phys. A **386**, 79 (1982).

[20] S. Goriely, M. Samyn, J. M. Pearson, and M. Onsi, Further explorations of Skyrme-Hartree-Fock-Bogoliubov mass formulas. IV: Neutron-matter constraint, Nucl. Phys. A **750**, 425 (2005).

[21] M. Kortelainen, T. Lesinski, J. Moré, W. Nazarewicz, J. Sarich, N. Schunck, M. V. Stoitsov, and S. Wild, Nuclear energy density optimization, Phys. Rev. C **82**, 024313 (2010).

[22] M. Kortelainen, J. McDonnell, W. Nazarewicz, P.-G. Reinhard, J. Sarich, N. Schunck, M. V. Stoitsov, and S. M. Wild, Nuclear energy density optimization: Large deformations, Phys. Rev. C **85**, 024304 (2012).

[23] M. Kortelainen, J. McDonnell, W. Nazarewicz, E. Olsen, P.-G. Reinhard, J. Sarich, N. Schunck, S. M. Wild, D. Davesne, J. Erler, and A. Pastore, Nuclear energy density optimization: Shell structure, Phys. Rev. C **89**, 054314 (2014).

[24] S. Shen, G. Colò, and X. Roca-Maza, Skyrme functional with tensor terms from *ab initio* calculations of neutron-proton drops, Phys. Rev. C **99**, 034322 (2019).

[25] X. Roca-Maza, M. Brenna, B. K. Agrawal, P. F. Bortignon, G. Colò, L.-G. Cao, N. Paar, and D. Vretenar, Giant quadrupole resonances in ^{208}Pb, the nuclear symmetry energy, and the neutron skin thickness, Phys. Rev. C **87**, 034301 (2013).

[26] X. Roca-Maza, private communication.

[27] J. Dobaczewski, H. Flocard, and J. Treiner, Hartree-Fock-Bogolyubov description of nuclei near the neutron-drip line, Nucl. Phys. A **422**, 103 (1984).

[28] R. N. Perez, N. Schunck, R.-D. Lasseri, C. Zhang, and J. Sarich, Axially deformed solution of the Skyrme-Hartree-Fock-Bogolyubov equations using the transformed harmonic oscillator basis (III) HFBTHO (v3.00): A new version of the program, Comput. Phys. Commun. **220**, 363 (2017).

[29] T. Nikšić, D. Vretenar, and P. Ring, Relativistic nuclear energy density functionals: Adjusting parameters to binding energies, Phys. Rev. C **78**, 034318 (2008).

[30] G. A. Lalazissis, T. Nikšić, D. Vretenar, and P. Ring, New relativistic mean-field interaction with density-dependent meson-nucleon couplings, Phys. Rev. C **71**, 024312 (2005).

[31] W. Long, J. Meng, N. Van Giai, and S.-G. Zhou, New effective interactions in relativistic mean field theory with nonlinear terms and density-dependent meson-nucleon coupling, Phys. Rev. C **69**, 034319 (2004).

[32] B. Wei, Q. Zhao, Z.-H. Wang, J. Geng, B.-Y. Sun, Y.-F. Niu, and W.-H. Long, Novel relativistic mean field Lagrangian guided by pseudo-spin symmetry restoration, Chin. Phys. C **44**, 074107 (2020).

[33] W. H. Long, H. Sagawa, J. Meng, and N. Van Giai, Evolution of nuclear shell structure due to the pion exchange potential, Europhys. Lett. **82**, 12001 (2008).

[34] W. H. Long, H. Sagawa, N. V. Giai, and J. Meng, Shell structure and ρ-tensor correlations in density dependent relativistic Hartree-Fock theory, Phys. Rev. C **76**, 034314 (2007).

[35] Z. Wang, T. Naito, and H. Liang, Tensor-force effects on shell-structure evolution in $N = 82$ isotones and $Z = 50$ isotopes in the relativistic Hartree-Fock theory, Phys. Rev. C **103**, 064326 (2021).

[36] Y. Tian, Z. Y. Ma, and P. Ring, A finite range pairing force for density functional theory in superfluid nuclei, Phys. Lett. B **676**, 44 (2009).

[37] J. Dobaczewski, W. Nazarewicz, T. R. Werner, J. F. Berger, C. R. Chinn, and J. Dechargé, Mean-field description of ground-state properties of drip-line nuclei: Pairing and continuum effects, Phys. Rev. C **53**, 2809 (1996).

[38] H. Nakada and M. Yamagami, Coulombic effect and renormalization in nuclear pairing, Phys. Rev. C **83**, 031302(R) (2011).

[39] P. A. Zyla, R. M. Barnett, J. Beringer, O. Dahl, D. A. Dwyer, D. E. Groom, C.-J. Lin, K. S. Lugovsky, E. Pianori, D. J. Robinson, C. G. Wohl, W.-M. Yao, K. Agashe, G. Aielli, B. C. Allanach, C. Amsler, M. Antonelli, E. C. Aschenauer, D. M. Asner, H. Baer *et al.* (Particle Data Group), Review of particle physics, Prog. Theor. Exp. Phys. **2020**, 083C01 (2020).

[40] T. Naito, G. Colò, H. Liang, and X. Roca-Maza, Second and fourth moments of the charge density and neutron-skin thickness of atomic nuclei, Phys. Rev. C **104**, 024316 (2021).

[41] C. Gorges, L. V. Rodríguez, D. L. Balabanski, M. L. Bissell, K. Blaum, B. Cheal, R. F. Garcia Ruiz, G. Georgiev, W. Gins, H. Heylen, A. Kanellakopoulos, S. Kaufmann, M. Kowalska, V. Lagaki, S. Lechner, B. Maaß, S. Malbrunot-Ettenauer, W. Nazarewicz, R. Neugart, G. Neyens *et al.*, Laser Spectroscopy of Neutron-Rich Tin Isotopes: A Discontinuity in Charge Radii across the $N = 82$ Shell Closure, Phys. Rev. Lett. **122**, 192502 (2019).

[42] J. M. Pearson and M. Farine, Relativistic mean-field theory and a density-dependent spin-orbit Skyrme force, Phys. Rev. C **50**, 185 (1994).

[43] B. S. Pudliner, A. Smerzi, J. Carlson, V. R. Pandharipande, S. C. Pieper, and D. G. Ravenhall, Neutron Drops and Skyrme Energy-Density Functionals, Phys. Rev. Lett. **76**, 2416 (1996).

[44] M. Bender, P.-H. Heenen, and P.-G. Reinhard, Self-consistent mean-field models for nuclear structure, Rev. Mod. Phys. **75**, 121 (2003).

[45] Y. Kanada-En'yo, Effects of density-dependent spin-orbit interactions in Skyrme-Hartree-Fock-Bogoliubov calculations of the charge radii and densities of Pb isotopes, arXiv:2209.11411 [nucl-th] (2022).

[46] M. M. Sharma, G. Lalazissis, J. König, and P. Ring, Isospin Dependence of the Spin-Orbit Force and Effective Nuclear Potentials, Phys. Rev. Lett. **74**, 3744 (1995).

[47] P.-G. Reinhard, The relativistic mean-field description of nuclei and nuclear dynamics, Rep. Prog. Phys. **52**, 439 (1989).

[48] M. Onsi, R. C. Nayak, J. M. Pearson, H. Freyer, and W. Stocker, Skyrme representation of a relativistic spin-orbit field, Phys. Rev. C **55**, 3166 (1997).

[49] R. C. Nayak and J. M. Pearson, Spin-orbit field and extrapolated properties of exotic nuclei, Phys. Rev. C **58**, 878 (1998).

[50] J. M. Pearson, Skyrme Hartree–Fock method and the spin–orbit term of the relativistic mean field, Phys. Lett. B **513**, 319 (2001).

[51] J. Geng, J. J. Li, W. H. Long, Y. F. Niu, and S. Y. Chang, Pseudospin symmetry restoration and the in-medium balance between nuclear attractive and repulsive interactions, Phys. Rev. C **100**, 051301(R) (2019).

[52] H. Liang, J. Meng, and S.-G. Zhou, Hidden pseudospin and spin symmetries and their origins in atomic nuclei, Phys. Rep. **570**, 1 (2015).

[53] A. V. Afanasjev, Band terminations in density functional theory, Phys. Rev. C **78**, 054303 (2008).

[54] W. Satuła, R. A. Wyss, and M. Zalewski, Contradicting effective mass scalings in the single-particle spectra calculated using the Skyrme energy density functional method, Phys. Rev. C **78**, 011302(R) (2008).

[55] R. F. Garcia Ruiz, M. L. Bissell, K. Blaum, A. Ekström, N. Frömmgen, G. Hagen, M. Hammen, K. Hebeler, J. D. Holt, G. R. Jansen, M. Kowalska, K. Kreim, W. Nazarewicz, R. Neugart, G. Neyens, W. Nörtershäuser, T. Papenbrock, J. Papuga, A. Schwenk, J. Simonis *et al.*, Unexpectedly large charge radii of neutron-rich calcium isotopes, Nat. Phys. **12**, 594 (2016).

[56] A. J. Miller, K. Minamisono, A. Klose, D. Garand, C. Kujawa, J. D. Lantis, Y. Liu, B. Maaß, P. F. Mantica, W. Nazarewicz, W. Nörtershäuser, S. V. Pineda, P.-G. Reinhard, D. M. Rossi, F. Sommer, C. Sumithrarachchi, A. Teigelhöfer, and J. Watkins, Proton superfluidity and charge radii in proton-rich calcium isotopes, Nat. Phys. **15**, 432 (2019).

[57] H. Sagawa, S. Yoshida, T. Naito, T. Uesaka, J. Zenihiro, J. Tanaka, and T. Suzuki, Isovector density and isospin impurity in ^{40}Ca, Phys. Lett. B **829**, 137072 (2022).

[58] Z.-X. Yang, X.-H. Fan, T. Naito, Z.-M. Niu, Z.-P. Li, and H. Liang, Calibration of nuclear charge density distribution by back-propagation neural networks, arXiv:2205.15649 [nucl-th] (2022).

[59] A. V. Afanasjev and E. Litvinova, Impact of collective vibrations on quasiparticle states of open-shell odd-mass nuclei and possible interference with the tensor force, Phys. Rev. C **92**, 044317 (2015).

[60] S. Kubis and M. Kutschera, Nuclear matter in relativistic mean field theory with isovector scalar meson, Phys. Lett. B **399**, 191 (1997).

[61] B. Liu, V. Greco, V. Baran, M. Colonna, and M. Di Toro, Asymmetric nuclear matter: The role of the isovector scalar channel, Phys. Rev. C **65**, 045201 (2002).

[62] X. Roca-Maza, X. Viñas, M. Centelles, P. Ring, and P. Schuck, Relativistic mean-field interaction with density-dependent meson-nucleon vertices based on microscopical calculations, Phys. Rev. C **84**, 054309 (2011).

[63] S. A. Fayans, Towards a universal nuclear density functional, Jetp Lett. **68**, 169 (1998).

[64] P.-G. Reinhard and W. Nazarewicz, Toward a global description of nuclear charge radii: Exploring the Fayans energy density functional, Phys. Rev. C **95**, 064328 (2017).

[65] C. A. Bertulani, H. F. Lü, and H. Sagawa, Odd-even mass difference and isospin dependent pairing interaction, Phys. Rev. C **80**, 027303 (2009).

[66] C. A. Bertulani, H. Liu, and H. Sagawa, Global investigation of odd-even mass differences and radii with isospin-dependent pairing interactions, Phys. Rev. C **85**, 014321 (2012).

[67] M. Yamagami, J. Margueron, H. Sagawa, and K. Hagino, Isoscalar and isovector density dependence of the pairing functional determined from global fitting, Phys. Rev. C **86**, 034333 (2012).

[68] H. Sagawa, Y. Tanimura, and K. Hagino, Competition between $T = 1$ and $T = 0$ pairing in pf-shell nuclei with $N = Z$, Phys. Rev. C **87**, 034310 (2013).

[69] K. Yoshida, Spin–Isospin response of deformed neutron-rich nuclei in a self-consistent Skyrme energy-density-functional approach, Prog. Theor. Exp. Phys. **2013**, 113D02 (2013).

[70] H. Sagawa, C. L. Bai, and G. Colò, Isovector spin-singlet ($T = 1, S = 0$) and isoscalar spin-triplet ($T = 0, S = 1$) pairing interactions and spin-isospin response, Phys. Scr. **91**, 083011 (2016).

[71] S. Teeti and A. V. Afanasjev, Global study of separable pairing interaction in covariant density functional theory, Phys. Rev. C **103**, 034310 (2021).

[72] T. Oishi, G. Kružić, and N. Paar, Role of residual interaction in the relativistic description of M1 excitation, J. Phys. G: Nucl. Part. Phys. **47**, 115106 (2020).

[73] T. Oishi, G. Kružić, and N. Paar, Discerning nuclear pairing properties from magnetic dipole excitation, Eur. Phys. J. A **57**, 180 (2021).

[74] K. Yoshida and Y. Tanimura, Spin-triplet proton-neutron pair in spin-dipole excitations, Phys. Rev. C **104**, 014319 (2021).

[75] G. F. Bertsch, C. A. Bertulani, W. Nazarewicz, N. Schunck, and M. V. Stoitsov, Odd-even mass differences from self-consistent mean field theory, Phys. Rev. C **79**, 034306 (2009).

[76] L. M. Robledo, R. Bernard, and G. F. Bertsch, Pairing gaps in the Hartree-Fock-Bogoliubov theory with the Gogny D1S interaction, Phys. Rev. C **86**, 064313 (2012).

[77] C. J. Horowitz and J. Piekarewicz, Impact of spin-orbit currents on the electroweak skin of neutron-rich nuclei, Phys. Rev. C **86**, 045503 (2012).

[78] P.-G. Reinhard and W. Nazarewicz, Nuclear charge densities in spherical and deformed nuclei: Toward precise calculations of charge radii, Phys. Rev. C **103**, 054310 (2021).